PROCEEDINGS A

royalsocietypublishing.org/journal/rspa

Research

Cite this article: Pozzi M, Marconi J, Jain S, Li M, Braghin F. 2025 Adjoint sensitivities for the optimization of nonlinear structural dynamics via spectral submanifolds. *Proc. R. Soc. A* **481**: 20250244.
https://doi.org/10.1098/rspa.2025.0244

Received: 20 March 2025
Accepted: 28 October 2025

Subject Areas:
computational mechanics, microsystems, structural engineering

Keywords:
nonlinear dynamics, shape optimization, topology optimization, adjoint method, reduced-order models, spectral submanifolds

Author for correspondence:
Jacopo Marconi
e-mail: jacopo.marconi@polimi.it

Adjoint sensitivities for the optimization of nonlinear structural dynamics via spectral submanifolds

Matteo Pozzi[1], Jacopo Marconi[1], Shobhit Jain[2], Mingwu Li[3,4] and Francesco Braghin[1]

[1]Department of Mechanical Engineering, Politecnico di Milano, Via G. La Masa 1, Milan 20156, Italy
[2]Delft Institute of Applied Mathematics, TU Delft, Mekelweg 4, Delft, ZH 2628CD, The Netherlands
[3]Department of Mechanics and Aerospace Engineering, Southern University of Science and Technology, Shenzhen, 518055, People's Republic of China
[4]State Key Laboratory of Structural Analysis, Optimization and CAE Software for Industrial Equipment, Dalian University of Technology, Dalian 116024, People's Republic of China

MP, 0009-0003-8337-8219; JM, 0000-0003-1115-3857; ML, 0000-0002-3570-6535

This work presents an optimization framework for tailoring the nonlinear dynamic response of lightly damped mechanical systems using spectral submanifold (SSM) reduction. We derive the SSM-based backbone curve and its sensitivity with respect to parameters up to arbitrary polynomial orders, enabling efficient and accurate optimization of the nonlinear frequency–amplitude relation. Sensitivity expressions are obtained via the adjoint method, which significantly reduces computational cost compared to direct differentiation as the number of parameters increases. A key feature of the framework is the automatic adjustment of the expansion order of SSM-based reduced-order models using user-defined error tolerances during optimization. We demonstrate the effectiveness of the approach through several numerical examples, including the first application of topology optimization in nonlinear structural dynamics via arbitrary-order SSMs. Hence, the

THE ROYAL SOCIETY PUBLISHING

proposed framework extends the applicability of SSM-based optimization to practical engineering problems, providing a robust tool for designing and optimizing nonlinear mechanical structures.

1. Introduction

The importance of considering nonlinear effects in the design phase has been widely demonstrated by the growing number of applications where nonlinearities are not merely a side effect to be avoided but play a functional role. Notable examples include frequency division [1], vibration mitigation [2], nonlinear energy sinks and targeted energy transfer [3], micro- and nanomechanical resonators [4,5] and microelectromechanical sensors [6,7].

The increasing complexity of nonlinear applications has driven the advancement of analytical and computational tools in the field of reduced-order models [8,9] for analysing the dynamic behaviour of nonlinear mechanical systems. A common approach involves computing the frequency–amplitude relation of a nonlinear normal mode [10,11] through *backbone curves* (e.g. [12]). These curves are typically obtained using numerical continuation techniques with the collocation method [13], the harmonic balance method (HBM) [14] or the shooting method [15]. Alternatively, *backbone curves* can be derived from the reduced dynamics on the spectral submanifold (SSM), which has proven particularly effective for high-dimensional mechanical systems [16,17].

The variety of numerical methods, along with the ever-growing interest in nonlinear applications, has provided an excellent playground for developing optimization techniques aimed at tailoring the nonlinear dynamic response of mechanical systems. For instance, approaches based on the nonlinear normal modes and the HBM have been used to optimize for the hardening behaviour in resonators and plane frame structures [18–20]. Similarly, shape optimization has been applied to adjust eigenfrequencies and modal coupling coefficients in geometrically nonlinear microelectromechanical system (MEMS) gyroscopes [21,22]. Other strategies include nonlinear synthesis for tailoring the backbone curve [23] and gradient-free optimization [24]. In the field of topology optimization [25], the equivalent static load method [26] has been used by [27–29], while [30,31] carried out eigenvalue optimization with frequency-dependent material properties.

Despite these advancements, tailoring the nonlinear dynamic response of a system remains a significant challenge. This is mainly due to the difficulties of the numerical methods in handling high-dimensional systems with a large number of parameters. In addition, these optimization approaches are highly sensitive to user-defined parameters, such as the number of harmonics in the HBM or the arc-length parameter in numerical continuation. As the system behaviour evolves throughout the optimization process, these parameters may require adjustment to ensure accuracy and convergence. Moreover, inherent limitations of the numerical methods, particularly in HBM sensitivity analysis, can influence the reliability of the optimization results [32].

Recently, Pozzi *et al.* [33] demonstrated the benefits of using SSM-based reduced-order models in optimization routines. A key advantage of this approach is the availability of analytical expressions for both the backbone curve and its sensitivity, enabling more efficient and accurate optimization. In addition, the SSM reduction process requires only a single user-defined parameter, the expansion order, which can be automatically adjusted during the optimization based on the residual of the invariance equation. However, in this work [33], the sensitivities were still computed via direct differentiation, which is computationally demanding as the number of optimization parameters increases. Moreover, the SSM formulation was based on tensor notation [16], which is not the most computationally efficient choice for approximating multivariate polynomials. The second issue can be addressed by employing the multi-index notation [17], which has been proven to be more efficient than the tensor approach. This has been shown in [34], where the authors applied topology optimization to tailor the hardening/softening dynamic

Table 1. Synoptic view of the main contributions in invariant manifold based sensitivities, considering whether the method targets a conservative or a general (non-conservative) system, which notation is used, whether direct differentiation (DD) or adjoint method (AM) sensitivities are employed, the manifold expansion order, the considered space for sensitivities and objective functions, and if parametric/topology optimization problems (PO/TO) are considered.

reference	system	notation	sensitivity	order	space	optim.
Pozzi *et al.* [33]	cons.	tensor	DD	arbitrary	physical	PO
Li [35]	general	multi-index	DD, AM[a]	3	reduced	n.a.
Pozzi *et al.* [34]	cons.	multi-index	AM	3	reduced	TO
This contribution	general	multi-index	DD, **AM**	**arbitrary**	**physical**	PO, TO

[a]The AM implementation of [35] is sensibly less efficient than the one presented in the current work.

response of conservative, nonlinear mechanical systems. By utilizing the adjoint sensitivity expressions derived in [35], simplified to the undamped case, the approach was successfully applied to a system with 20 000 design variables and around 40 000 degrees of freedom. However, the explicit formulation used in [34] is limited to cubic-order computation of the Lyapunov subcentre manifold in conservative systems.[1] Furthermore, this method focuses on tailoring the backbone curve in the *reduced space*, which does not allow for an optimization of the frequency–amplitude relation in physical coordinates. Indeed, the shape of backbone curves in physical and reduced coordinates can differ significantly, as the latter depends on the choice of parametrization [16].

(i) Our contribution

In this work, we propose an automatic and efficient procedure to compute the sensitivities of invariant manifolds, specifically SSMs, up to an arbitrary expansion order, leveraging the adjoint method. The central contribution of our work is to make previously intractable sensitivity analyses feasible for large-scale finite element structures with a high number of parameters. In addition to this scalability, our approach enables the computation of sensitivities for both the reduced dynamics and the parametrization linking reduced and physical coordinates at any desired order. This, in turn, allows optimization objectives to be defined directly in the physical space, a highly desirable feature for practical engineering applications.

To achieve these results, in addition to adopting the multi-index notation (appendix B), we develop mathematical expressions for adjoint sensitivities up to arbitrary orders (appendices E and G). A summary of these methodological contributions and their distinctions from previous approaches is listed in table 1. We then demonstrate the computational benefits of this mathematical formulation over several numerical examples featuring multi-parameter as well as topology optimization applications (§5).

(ii) Paper outline

The rest of the paper is organized as follows: §§2 and 3 introduce the mechanical system under consideration and outline the procedure for computing the SSM and the backbone curve. Section 4 then presents the expressions for the backbone curve sensitivity using the adjoint method. For comparison, the sensitivity derived through direct differentiation is also provided in appendix E. Finally, §5 showcases numerical examples to validate the proposed sensitivity formulations. Section 6 closes the paper with the conclusions and outlines future research directions.

[1]In the absence of damping and internal resonances, the SSM formulation reduces to that of the associated Lyapunov subcentre manifold.

royalsocietypublishing.org/journal/rspa Proc. R. Soc. A 481: 20250244

2. Mechanical system

Consider the equation of motion of a lightly damped, autonomous, nonlinear mechanical system:

$$\mathbf{M}\ddot{\boldsymbol{x}} + \mathbf{C}\boldsymbol{x} + \mathbf{K}\boldsymbol{x} + \boldsymbol{f}(\boldsymbol{x}) = \mathbf{0}, \tag{2.1}$$

where $\boldsymbol{x} \in \mathbb{R}^n$ is the state vector, n is the number of degrees of freedom, $\mathbf{M}$, $\mathbf{C}$ and $\mathbf{K}$ are the mass, damping, and stiffness matrices (all belonging to $\mathbb{R}^{n\times n}$), respectively, and $\boldsymbol{f} \in \mathbb{R}^n$ is the vector of displacement-dependent nonlinear force. In this work, $\boldsymbol{f}$ contains the contribution of quadratic and cubic nonlinearities in the displacement,

$$\boldsymbol{f}(\boldsymbol{x}) = \boldsymbol{f}_2(\boldsymbol{x},\boldsymbol{x}) + \boldsymbol{f}_3(\boldsymbol{x},\boldsymbol{x},\boldsymbol{x}), \tag{2.2}$$

and represents the contribution of the internal nonlinear elastic forces. These are efficiently managed using the tensor notation [36] as

$$f^i = T_2^{ijk} x^j x^k + T_3^{ijkl} x^j x^k x^l, \tag{2.3}$$

where f^i is the ith element of $\boldsymbol{f}$, and the tensors $T_2 \in \mathbb{R}^{n\times n\times n}$ and $T_3 \in \mathbb{R}^{n\times n\times n\times n}$ contain the coefficients of the quadratic and cubic nonlinearities. Notice that we denote the components of a vector or a tensor using superscripts (not to be confused with exponents).

The damping matrix $\mathbf{C}$ is computed using the Rayleigh damping formulation:

$$\mathbf{C} = \alpha_R \mathbf{M} + \beta_R \mathbf{K}, \tag{2.4}$$

where α_R and β_R are non-negative coefficients (see appendix A for more details on the choice of the damping coefficients).

The second-order system equation (2.1) is transformed into the first-order form:

$$\mathbf{B}\dot{\boldsymbol{z}} = \mathbf{A}\boldsymbol{z} + \boldsymbol{F}(\boldsymbol{z}), \tag{2.5}$$

where

$$\boldsymbol{z} = \begin{bmatrix} \boldsymbol{x} \\ \dot{\boldsymbol{x}} \end{bmatrix}, \quad \mathbf{B} = \begin{bmatrix} \mathbf{C} & \mathbf{M} \\ \mathbf{M} & \mathbf{0} \end{bmatrix}, \quad \mathbf{A} = \begin{bmatrix} -\mathbf{K} & \mathbf{0} \\ \mathbf{0} & \mathbf{M} \end{bmatrix}, \quad \boldsymbol{F}(\boldsymbol{z}) = \begin{bmatrix} -\boldsymbol{f}(\boldsymbol{x}) \\ \mathbf{0} \end{bmatrix}. \tag{2.6}$$

Assume that system (2.5) has a stable and hyperbolic fixed point at $\boldsymbol{z} = \mathbf{0}$. The eigenvalues $\lambda_i \in \mathbb{C}$ of such a system are computed by solving the generalized right and left eigenvalue problems:

$$(\mathbf{A} - \lambda_i \mathbf{B})\boldsymbol{v}_i = \mathbf{0} \quad \text{and} \quad \boldsymbol{u}_i^*(\mathbf{A} - \lambda_i \mathbf{B}) = \mathbf{0}, \tag{2.7}$$

where $(\bullet)^*$ represents the conjugate transpose operator, and $\boldsymbol{v}_i \in \mathbb{C}^{2n}$ and $\boldsymbol{u}_i \in \mathbb{C}^{2n}$ are the right and left eigenvectors associated to λ_i.

The eigenvalues and eigenvectors of the first-order system (computed from equation (2.7)) can be related to those of the respective undamped second-order system as

$$\lambda_1 = \bar{\lambda}_2 = \lambda = -\xi\omega + \mathrm{i}\omega\sqrt{1-\xi^2} = \alpha + \mathrm{i}\omega_d \tag{2.8}$$

and

$$\boldsymbol{v}_1 = \bar{\boldsymbol{v}}_2 = \begin{bmatrix} \boldsymbol{\varphi} \\ \lambda\boldsymbol{\varphi} \end{bmatrix}, \quad \boldsymbol{u}_1 = \bar{\boldsymbol{u}}_2 = \begin{bmatrix} \boldsymbol{\varphi} \\ \bar{\lambda}\boldsymbol{\varphi} \end{bmatrix}, \tag{2.9}$$

where $\boldsymbol{\varphi} \in \mathbb{R}^n$ and $\omega \in \mathbb{R}$ are obtained from the generalized eigenvalue problem

$$(\mathbf{K} - \omega^2 \mathbf{M})\boldsymbol{\varphi} = \mathbf{0}, \tag{2.10}$$

where the mode shapes $\boldsymbol{\varphi}$ are assumed to be mass normalized, yielding

$$\boldsymbol{\varphi}^T \mathbf{M} \boldsymbol{\varphi} = 1 \quad \text{and} \quad \boldsymbol{\varphi}^T \mathbf{K} \boldsymbol{\varphi} = \omega^2. \tag{2.11}$$

Using the definition of the damping matrix and the mass normalization condition (equations (2.4) and (2.11)), the damping ratio of the system is defined as

$$\xi = \frac{\boldsymbol{\varphi}^T \mathbf{C} \boldsymbol{\varphi}}{2\omega} = \frac{\alpha_R + \beta_R \omega^2}{2\omega}. \tag{2.12}$$

For lightly damped systems, we require that $\xi \ll 1$.

3. SSM computation

We provide here the basic steps used to compute the *two-dimensional* SSM for an autonomous, damped, nonlinear mechanical system (see [16,17] for a complete analysis).

Call E the two-dimensional master subspace spanned by $\boldsymbol{v}_1$ and $\boldsymbol{v}_2$. Let $\boldsymbol{R} : \mathbb{C}^2 \to \mathbb{C}^2$ be a two-dimensional parametrization of the reduced dynamics, such that

$$\dot{\boldsymbol{p}} = \boldsymbol{R}(\boldsymbol{p}), \tag{3.1}$$

where $\boldsymbol{p} \in \mathbb{C}^2$ is the vector of reduced coordinates. Using $\boldsymbol{p}$, let $\boldsymbol{W} : \mathbb{C}^2 \to \mathbb{R}^{2n}$ be a parametrization of the SSM attached to the master subspace E. Then, the state vector $\boldsymbol{z}$ can be expressed as

$$\boldsymbol{z} = \boldsymbol{W}(\boldsymbol{p}) = \begin{bmatrix} \boldsymbol{w}(\boldsymbol{p}) \\ \dot{\boldsymbol{w}}(\boldsymbol{p}) \end{bmatrix}, \tag{3.2}$$

where $\boldsymbol{w}(\boldsymbol{p})$ and $\dot{\boldsymbol{w}}(\boldsymbol{p})$ are the parametrizations for the displacement $\boldsymbol{x}$ and for the velocity $\dot{\boldsymbol{x}}$, respectively.

Substituting the parameterizations (3.1) and (3.2) into equation (2.5), we obtain the *autonomous invariance equation*:

$$\mathbf{B} \frac{\partial \boldsymbol{W}(\boldsymbol{p})}{\partial \boldsymbol{p}} \boldsymbol{R}(\boldsymbol{p}) = \mathbf{A} \boldsymbol{W}(\boldsymbol{p}) + \boldsymbol{F}(\boldsymbol{W}(\boldsymbol{p})). \tag{3.3}$$

To numerically solve equation (3.3), the parameterizations (3.1) and (3.2) are Taylor expanded up to a given order M:

$$\boldsymbol{R}(\boldsymbol{p}) \approx \sum_{\substack{\boldsymbol{m} \in \mathbb{N}^2 \\ m < M}} \boldsymbol{R}_{\boldsymbol{m}} \boldsymbol{p}^{\boldsymbol{m}}, \quad \boldsymbol{w}(\boldsymbol{p}) \approx \sum_{\substack{\boldsymbol{m} \in \mathbb{N}^2 \\ m < M}} \boldsymbol{w}_{\boldsymbol{m}} \boldsymbol{p}^{\boldsymbol{m}}, \quad \dot{\boldsymbol{w}}(\boldsymbol{p}) \approx \sum_{\substack{\boldsymbol{m} \in \mathbb{N}^2 \\ m < M}} \dot{\boldsymbol{w}}_{\boldsymbol{m}} \boldsymbol{p}^{\boldsymbol{m}}, \tag{3.4}$$

where the multi-index notation is used to express the multivariate polynomials (see appendix B). The terms $\boldsymbol{R}_{\boldsymbol{m}} = \{R^1_{\boldsymbol{m}}, R^2_{\boldsymbol{m}}\}^T \in \mathbb{C}^2$ are the coefficients of the reduced dynamics, while $\boldsymbol{w}_{\boldsymbol{m}} \in \mathbb{C}^n$ and $\dot{\boldsymbol{w}}_{\boldsymbol{m}} \in \mathbb{C}^n$ are the manifold coefficients.

Following the approach described in [17], it is possible to split the *autonomous invariance equation* into many *cohomological equations*, one for each multi-index $\boldsymbol{m}$:

$$\mathbf{L}_{\boldsymbol{m}} \boldsymbol{w}_{\boldsymbol{m}} = \boldsymbol{h}_{\boldsymbol{m}}, \tag{3.5}$$

$$\mathbf{L}_{\boldsymbol{m}} = \mathbf{K} + \Lambda_{\boldsymbol{m}} \mathbf{C} + \Lambda^2_{\boldsymbol{m}} \mathbf{M}, \tag{3.6}$$

$$\Lambda_{\boldsymbol{m}} = \boldsymbol{m} \cdot \boldsymbol{\Lambda} \tag{3.7}$$

and

$$\boldsymbol{h}_{\boldsymbol{m}} = \boldsymbol{D}_{\boldsymbol{m}} \boldsymbol{R}_{\boldsymbol{m}} + \boldsymbol{C}_{\boldsymbol{m}}, \tag{3.8}$$

where $\boldsymbol{\Lambda} = \{\lambda_1, \lambda_2\}^T$, while $\boldsymbol{C}_{\boldsymbol{m}} \in \mathbb{C}^n$ and $\boldsymbol{D}_{\boldsymbol{m}} \in \mathbb{C}^{n \times 2}$ are defined in appendix D; $\boldsymbol{C}_{\boldsymbol{m}}$, in particular, depends on the parametrization coefficients at orders lower than m.

Equation (3.5) is solved up to any arbitrary expansion order for the manifold coefficients $\boldsymbol{w}_{\boldsymbol{m}}$, starting from the first. At each order m, there are $m+1$ distinct multi-indices. Details on the computation of $\boldsymbol{R}_{\boldsymbol{m}}$ and $\dot{\boldsymbol{w}}_{\boldsymbol{m}}$ are given in appendix D. Here, we just mention that the coefficients $\boldsymbol{R}_{\boldsymbol{m}}$ are obtained following the normal-form style parametrization [17], for which the coefficients are non-zero only if the near-resonance condition is satisfied (see appendix C). This allows us to write an *analytical expression* for the backbone curve [33].

(a) Backbone curve

Using the polar version of the reduced coordinates $\boldsymbol{p}(\vartheta) = \varrho\{e^{i\vartheta}, e^{-i\vartheta}\}^T$, it is possible to write an analytical expression for the backbone curve in the reduced space [33]:

$$\Omega(\varrho) = \mathrm{Im}\lambda + \sum_{m>1} \mathrm{Im}R^1_{\boldsymbol{m}}\varrho^{m-1}, \tag{3.9}$$

where the response frequency Ω is function of the reduced amplitude ϱ. According to the normal-form style parametrization [17], the coefficients $R^j_{\boldsymbol{m}}$ are non-zero if the multi-index $\boldsymbol{m}$ satisfies the near-resonance condition (appendix C). From this condition, it follows that the coefficients associated with even orders are always zero, meaning that the summation in equation (3.9) can be performed only on odd orders.

For the purposes of computing the sensitivities, the expression for Ω can be rewritten as

$$\Omega(\varrho) = \frac{1}{2}i(\lambda_2 - \lambda_1) + \frac{1}{2}i\sum_{m>1}(R^2_{\boldsymbol{m}} - R^1_{\boldsymbol{m}})\varrho^{m-1}. \tag{3.10}$$

While selecting the target frequency is straightforward, defining the 'amplitude' is less direct owing to multiple valid options (e.g. maximum value, amplitude of a spectral component, peak-to-peak amplitude). In this work, we define it as the RMS response of a selected degree of freedom. Call x^i the ith element of the vector $\boldsymbol{x}$, corresponding to the displacement of the ith degree of freedom. Similarly, let us call $w^i_{\boldsymbol{m}}$ the ith component of the vector $\boldsymbol{w}_{\boldsymbol{m}}$. This value can be computed using the manifold parametrization (equation (3.2)):

$$x^i(\varrho, \vartheta) = \sum_{\boldsymbol{m}} w^i_{\boldsymbol{m}}\boldsymbol{p}^{\boldsymbol{m}}(\varrho, \vartheta), \tag{3.11}$$

where x^i is a function of the reduced amplitude ϱ and of the phase ϑ. To remove the dependence on ϑ, we define a set of ϑ values as

$$\vartheta_k = k\frac{2\pi}{N_\vartheta} \quad \forall k = 1, \ldots, N_\vartheta. \tag{3.12}$$

Then, we compute the RMS of x^i over the values of ϑ_k, leading to

$$x(\varrho) = \sqrt{\frac{1}{N_\vartheta}\sum_{k=1}^{N_\vartheta}(x^i(\varrho, \vartheta_k))^2}. \tag{3.13}$$

In an optimization framework, this relation can be used to find the reduced amplitude ϱ corresponding to a target physical amplitude $x = x_0$. The obtained ϱ can then be used to evaluate the corresponding frequency Ω on the backbone from equation (3.10). This way, the frequency–amplitude relation can be tracked in the *physical* space.

4. Sensitivity analysis

As done in [33], we propose an optimization procedure to tailor the backbone curve by defining target points in terms of response frequency Ω and physical amplitude x. The optimization problem can be stated as

$$\begin{aligned} \min_{\boldsymbol{\mu}} \quad & J, \\ \text{s.t.} \quad & \Omega(\varrho(x_j)) - \Omega_j = 0, \quad \forall j, \\ & \boldsymbol{\mu}_L < \boldsymbol{\mu} < \boldsymbol{\mu}_U, \end{aligned} \tag{4.1}$$

where $\boldsymbol{\mu}$ is the vector of design variables with lower and upper bounds $\boldsymbol{\mu}_L$ and $\boldsymbol{\mu}_U$, respectively, J is the objective function (implicitly) depending on $\boldsymbol{\mu}$, and Ω_j is the jth target frequency corresponding to the target amplitude x_j.

To solve the optimization problem (equation (4.1)) using a gradient-based approach, the sensitivities of both the objective function J and the constraints must be computed. In particular, the sensitivity of the response frequency Ω depends on the SSM coefficients. A straightforward approach to obtain this sensitivity is the direct differentiation method, which involves applying the chain rule to differentiate all equations contributing to the computation of Ω. The detailed steps of this procedure are provided in appendix E. However, the computational cost of direct differentiation scales with the number of design variables, which can limit the size of the optimization problem.

To efficiently handle optimization problems with a large number of design variables, we instead compute the sensitivity of Ω using the adjoint method [37], in which the complex derivatives are managed through *Wirtinger calculus* [37,38].

(a) The adjoint method

The first step of the *adjoint method* is the identification of the *state variables* and the corresponding *state functions*. In this case, the *state variables* are the reduced amplitude ϱ, the manifold coefficients $\boldsymbol{w}_m$ for $m > 1$, the mode shape $\boldsymbol{\varphi}$ and the natural frequency ω. The corresponding *state functions* are the RMS of the physical amplitude (equation (3.13)), the cohomological equations (equation (D 11)), the generalized eigenvalue problem (equation (2.10)) and the mass normalization condition (equation (2.11)).

Next, the *Lagrangian function* is assembled as follows:

$$\mathcal{L} = \Omega + \zeta_\varrho(x - x_0) + \sum_{m>1} \boldsymbol{\zeta}_m^T(\mathbf{L}_m \boldsymbol{w}_m - \boldsymbol{h}_m) + \boldsymbol{\zeta}_{\boldsymbol{\varphi}}^T(\mathbf{K} - \omega^2\mathbf{M})\boldsymbol{\varphi} + \zeta_\omega(\boldsymbol{\varphi}^T\mathbf{M}\boldsymbol{\varphi} - 1), \tag{4.2}$$

where ζ_ϱ, $\boldsymbol{\zeta}_m$, $\boldsymbol{\zeta}_{\boldsymbol{\varphi}}$, and ζ_ω are the *adjoint variables*. According to *Wirtinger calculus* [37,38], only the real part of the cohomological equations should be used, as the Lagrangian must be a real-valued function. However, in this case, it can be shown that the sum of all cohomological equations inherently results in a real-valued function. This follows from the *symmetric multi-index* property (appendix B), which ensures that the cohomological equations appear in complex-conjugate pairs.

The *adjoint variables* are computed solving the *adjoint equations*, which are obtained by taking the partial derivatives of $\mathcal{L}$ with respect to the *state variables*:

$$\frac{\partial \mathcal{L}}{\partial \varrho} = \frac{\partial \Omega}{\partial \varrho} + \zeta_\varrho \frac{\partial x}{\partial \varrho} = 0, \tag{4.3}$$

$$\frac{\partial \mathcal{L}}{\partial \boldsymbol{w}_m} = \frac{\partial \Omega}{\partial \boldsymbol{w}_m} + \zeta_\varrho \frac{\partial x}{\partial \boldsymbol{w}_m} + \boldsymbol{\zeta}_m^T \mathbf{L}_m - \sum_{q>m} \boldsymbol{\zeta}_q^T \frac{\partial \boldsymbol{h}_q}{\partial \boldsymbol{w}_m} = \mathbf{0}^T, \tag{4.4}$$

$$\frac{\partial \mathcal{L}}{\partial \boldsymbol{\varphi}} = \frac{\partial \Omega}{\partial \boldsymbol{\varphi}} + \zeta_\varrho \frac{\partial x}{\partial \boldsymbol{\varphi}} - \sum_{m>1} \boldsymbol{\zeta}_m^T \frac{\partial \boldsymbol{h}_m}{\partial \boldsymbol{\varphi}} + \boldsymbol{\zeta}_{\boldsymbol{\varphi}}^T(\mathbf{K} - \omega^2\mathbf{M}) + 2\zeta_\omega \boldsymbol{\varphi}^T\mathbf{M} = \mathbf{0}^T \tag{4.5}$$

and

$$\frac{\partial \mathcal{L}}{\partial \omega} = \frac{\partial \Omega}{\partial \omega} + \sum_{m>1} \boldsymbol{\zeta}_m^T \left(\frac{\partial \mathbf{L}_m}{\partial \omega} \boldsymbol{w}_m - \frac{\partial \boldsymbol{h}_m}{\partial \omega} \right) - 2\omega \boldsymbol{\zeta}_{\boldsymbol{\varphi}}^T \mathbf{M}\boldsymbol{\varphi} = 0, \tag{4.6}$$

where the equations for $\boldsymbol{\zeta}_m$ are computed in reverse order, starting from the highest one, and the last two equations are solved together. All the partial derivatives involved in equations (4.3), (4.4), (4.5), and (4.6) are given in appendix G.

Using the adjoint variables, the sensitivity of Ω is obtained by taking the partial derivative of $\mathcal{L}$ with respect to all the design variables μ:

$$\frac{\partial \mathcal{L}}{\partial \mu} = \frac{\partial \Omega}{\partial \mu} + \sum_{m>1} \boldsymbol{\zeta}_m^T \left(\frac{\partial \mathbf{L}_m}{\partial \mu} \boldsymbol{w}_m - \frac{\partial \boldsymbol{h}_m}{\partial \mu} \right) + \boldsymbol{\zeta}_{\boldsymbol{\varphi}}^T \left(\frac{\partial \mathbf{K}}{\partial \mu} - \omega^2 \frac{\partial \mathbf{M}}{\partial \mu} \right) \boldsymbol{\varphi} + \zeta_\omega \boldsymbol{\varphi}^T \frac{\partial \mathbf{M}}{\partial \mu} \boldsymbol{\varphi}, \tag{4.7}$$

where the partial derivatives with respect to μ depend on how the system is parametrized, and they are usually straightforward to compute.

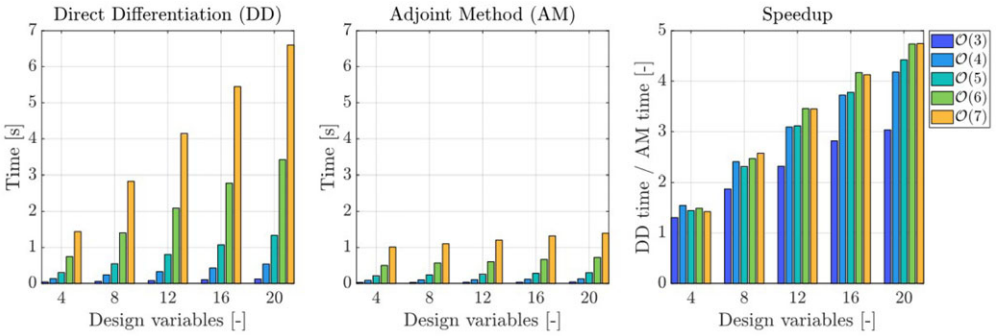

Figure 1. Computational times involved in the sensitivity analysis for a system with 501 degrees of freedom. The direct differentiation (left) and the adjoint method (centre) are compared for different SSM expansion orders and number of design variables. On the right, the speedup is shown.

It is important to point out that the *symmetric multi-index* property (appendix B) also holds for the adjoint variables $\boldsymbol{\zeta}_m$. In this way, we can avoid solving for nearly half of the adjoint equations associated with $\boldsymbol{\zeta}_m$.

Figure 1 illustrates the computational time involved in the sensitivity analysis. Specifically, the adjoint formulation is compared to the direct differentiation approach (outlined in appendix E) for a system with 501 degrees of freedom. The comparison is made for different SSM expansion orders and varying numbers of design variables. All computations were performed on a Windows workstation equipped with an Intel Core i9-13900KS CPU at 3.20 GHz and 128 GB of RAM at 4200 MT s^{-1}.

As expected, direct differentiation scales linearly with the number of design variables, while the adjoint method remains independent[2] of them, making it a more efficient approach for computing sensitivities. Specifically, direct differentiation requires solving one $n \times n$ linear system for each unique multi-index at every order and for each design variable. In contrast, the adjoint method requires solving only one such system per multi-index and order, regardless of the number of design variables.

For reference, computing the sensitivity using the direct differentiation approach for a system with 500 design variables, 1000 degrees of freedom, and an $\mathcal{O}(3)$ SSM takes 83.5 s, nearly 70 times longer than the adjoint method (see figure 8).

5. Numerical examples

In this section, four numerical examples are provided to highlight the advantages of the proposed adjoint sensitivity formulation. With the first one, we validate the adjoint sensitivity by approximating the perturbed backbone curve of two coupled nonlinear oscillators. Then, we utilize the sensitivity expression within a gradient-based optimization loop to tailor the backbone curve of nonlinear mechanical systems.

In all the optimization examples, the modal assurance criterion is used to identify and track the target mode shape throughout the optimization. This is required as the order of the modes may change during the optimization, thus leading to convergence issues if not properly addressed. See, for instance, [33,39] for more details about the modal assurance criterion.

The accuracy of the SSM reduction directly affects the reliability of the sensitivity analysis and, consequently, the overall optimization results. To ensure sufficient accuracy, we use the residual of the invariance equation (3.3) to define an error measure ε that quantifies the fidelity of the SSM

[2]The adjoint sensitivity (equation (4.7)) must be evaluated for each design variable, introducing a computational cost that scales linearly with their number. However, this overhead remains negligible compared to the linear scaling of direct differentiation.

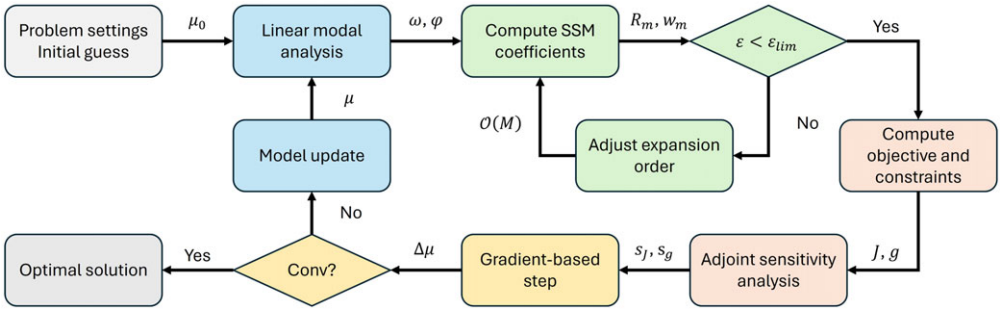

Figure 2. General scheme of the gradient-based optimization loop. Blue blocks represent the system model and linear modal analysis. Green blocks correspond to the SSM computation, including an inner loop that adjusts the expansion order to maintain reduction accuracy. Red blocks cover the evaluation of the objective function, constraints, and sensitivity computation (either via direct differentiation or adjoint method). Yellow blocks denote the optimization problem set-up and update steps.

approximation, following the approach in [33]. By specifying an error tolerance ε_{lim}, the expansion order of the SSM can be automatically increased until the residual error falls below the prescribed threshold.

However, for systems with strong nonlinearities, achieving the desired accuracy may require significantly higher expansion orders, resulting in substantial increases in computational cost. In such cases, the optimization process may become computationally prohibitive given limited resources. To mitigate this, a maximum allowable expansion order should be defined to prevent unbounded computational effort. If the required accuracy cannot be met within this limit, the optimization should either proceed or terminate with a warning indicating insufficient model accuracy.

All examples were implemented using YetAnotherFEcode v.1.4.0 [40] in MATLAB R2023b. The overall structure of the gradient-based optimization loop is shown in figure 2, where the inner accuracy loop is highlighted in green. For the parametric optimization problems, we used MATLAB's `fmincon` solver with the `interior-point` algorithm. For the topology optimization example, the method of moving asymptotes [41] was employed instead.

(a) Perturbed backbone of two coupled nonlinear oscillators

Consider the equations of motion of two coupled oscillators, with the first mass attached to the ground and to the second mass through nonlinear springs:

$$\left.\begin{aligned} &m\ddot{x}_1 + c\dot{x}_1 + k(2x_1 - x_2) + k_2x_1^2 + k_3x_1^3 + k_2(x_1 - x_2)^2 + k_3(x_1 - x_2)^3 = 0 \\ \text{and}\quad &m\ddot{x}_2 + c\dot{x}_2 + k(x_2 - x_1) + k_2(x_2 - x_1)^2 + k_3(x_2 - x_1)^3 = 0, \end{aligned}\right\} \tag{5.1}$$

where $m = 1$, $k = 1$, $k_2 = 0.5$ and $k_3 = 0.2$. The damping is computed according to Rayleigh damping with $\alpha_R = 0$ and $\beta_R = 0.1$, leading to a damping coefficient $c = \beta_R k = 0.1$. We focus on the displacement of the mass at the free end (x_2). The target mode shape is the first one, associated with eigenvalues $\lambda = -0.0191 \pm \mathrm{i}0.6177$. The SSM is expanded up to the fifth order.

First, the backbone curve of the system in nominal condition is computed (black lines in figure 3). Then, the sensitivities of the backbone curve with respect to the system parameters μ are computed using the adjoint method. These are used to make a prediction (cross markers in figure 3) of the backbone curve of the perturbed system as

$$\Omega(\mu + \delta\mu) = \Omega(\mu) + \frac{\partial\Omega}{\partial\mu}\delta\mu. \tag{5.2}$$

The predictions are then validated by actually computing the backbone curves of the perturbed system (coloured lines in figure 3). The natural frequency only changes owing to perturbations in

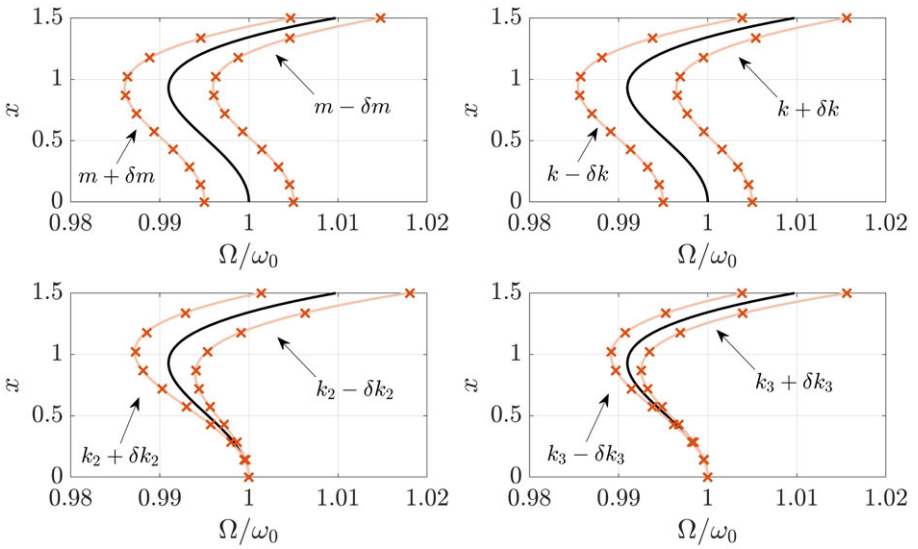

Figure 3. Nominal (black lines) and perturbed (coloured lines) backbone curves for the coupled oscillators. x is the RMS amplitude of x_2. The cross markers represent the predicted points obtained using the sensitivity values as in equation (5.2). In this example, the parameter perturbations are $\delta m = 0.01\,m$, $\delta k = 0.01\,k$, $\delta k_2 = 0.03\,k_2$ and $\delta k_3 = 0.03\,k_3$.

m and k, while perturbations in k_2 and k_3 become relevant at higher amplitudes, thus affecting the hardening/softening dynamic behaviour of the response.

Moreover, the results also show that the sensitivity-based predictions can be reliably used to study a system around its nominal parameters, making uncertainty quantification analysis extremely efficient [42].

(b) Optimization of a von Kármán beam

Consider a geometrically nonlinear, undamped, clamp–clamp von Kármán beam. This example provides a basis for comparing the proposed optimization approach, which uses multi-index notation to parametrize the manifold, with the method presented in [33], which employs tensorial notation. In both cases, the direct differentiation sensitivities, provided in [33] for the tensorial notation and in appendix E for the multi-index notation, are used.

The structure is described by a finite element model consisting of 10 von Kármán elements (27 degrees of freedom). As design variables, we take the beam thickness h, the length L and the amplitudes A_1 and A_2 which define the shape of the beam as

$$y = A_1 \sin\left(\frac{\pi x}{L}\right) + A_2 \sin\left(\frac{2\pi x}{L}\right),$$

with $x \in [0, L]$ and y the nodal coordinates of the beam. The material is characterized by Young's modulus (equal to 90 GPa), a Poisson's ratio of 0.3 and density corresponding to 7850 kg m^{-3}.

Initial values and bounds for the design variables are listed in table 2. The optimization problem is stated as follows:

$$\begin{aligned} \min_{\boldsymbol{\mu}} \quad & A_2 L, \\ \text{s.t.} \quad & \Omega(\varrho(v = 0.2\,h_0)) - \omega_0 = 0, \\ & \Omega(\varrho(v = 0.4\,h_0)) - 0.95\,\omega_0 = 0, \\ & \boldsymbol{\mu}_L \leq \boldsymbol{\mu} \leq \boldsymbol{\mu}_U, \end{aligned} \tag{5.3}$$

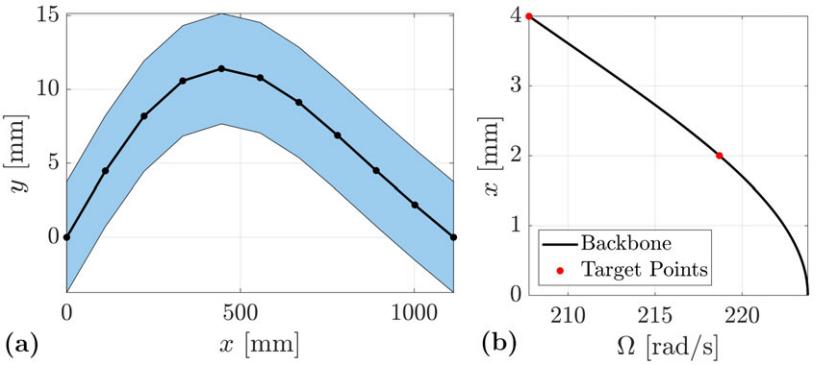

Figure 4. Optimal solution obtained solving problem (5.3). (a) Optimized beam shape. (b) Backbone curve corresponding to the optimal solution. The same results were obtained in [33] in 4.8 min, while here the computations took only 15 s.

Table 2. Initial values, lower bounds and upper bounds of the design variables for the von Kármán beam example.

design variable		initial value	lower bound	upper bound	optimal value
A_1	(mm)	0	0	20	10.7
A_2	(mm)	0	0	20	1.94
h	(mm)	10	1	100	7.49
L	(mm)	1000	500	1500	1113.6

Table 3. Optimal design variables obtained solving problem (5.6). The top row lists the lengths and widths of the drive and sense beams, as variations with respect to the initial values. The middle and bottom rows show the amplitudes of the top and bottom drive beams, respectively.

sizes (μm)	$\Delta l_d = 4.21$	$\Delta l_s = 0.04$	$\Delta w_d = -0.39$	$\Delta w_s = -0.25$	$\Delta w_c = 0.04$
top amp. (μm)	$A_1 = 0.00$	$A_2 = 1.58$	$A_3 = 0.02$	$A_4 = 0.79$	$A_5 = 0.06$
bottom amp. (μm)	$A_1 = 0.00$	$A_2 = 1.58$	$A_3 = 0.02$	$A_4 = 0.79$	$A_5 = 0.06$

where h_0 is the initial thickness, and ω_0 is the first eigenfrequency of the system (evaluated using the initial parameters); v is the y-displacement of the centre of the beam, which is also the d.f. we use to compute the backbone. In figure 4, x is the RMS amplitude of v.

Using the approach presented in [33], the optimization reaches convergence in 11 iterations. The overall computational time was approximately 4.8 min on a Windows laptop equipped with an Intel Core i7-1255U CPU at 1.70 GHz and 16 GB of RAM at 3200 MT s^{-1}. On the same machine, solving the same problem with the direct differentiation sensitivity (§4) yields identical results and optimization history (figure 4), but the process only takes approximately 15 s. This is because the multi-index notation is much more efficient than the tensorial one.

(c) Optimization of a MEMS gyroscope

Consider the MEMS gyroscope prototype [7] in figure 5. The drive (light red) and sense (light blue) frames are fixed throughout the optimization, as they host the actuation and sensing electrodes. Since the problem is two dimensional, each frame is modelled as a rigid mass with lumped inertial properties and 3 d.f. corresponding to the displacements and rotation of its centre of mass. On the other hand, the drive (red) and sense (blue) beams are represented by geometrically nonlinear von Kármán beams. The material is polysilicon [43], characterized by

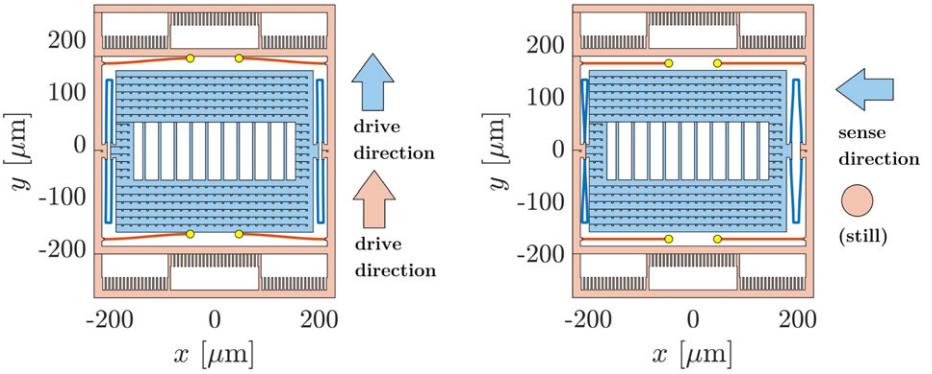

Figure 5. Drive (left) and sense (right) modes of the initial layout for the MEMS gyroscope. The folded beams (blue) are used to connect the drive frame (light red) to the sense mass (light blue), while the drive beams (red) connect the drive frame to the ground (yellow circles). Arrows show the displacements of the frame and the mass.

Young's modulus $E = 148\,\text{GPa}$, Poisson's ratio $\nu = 0.23$ and density $\varrho = 2330\,\text{kg}\,\text{m}^{-3}$. The Rayleigh damping parameters are $\alpha_R = 0.01$ and $\beta_R = 0$.

Using the multi point constraint approach [44, Ch. 13], each mass is connected to a node of the beam elements using the following *linearized* kinematic constraint:

$$\begin{bmatrix} u \\ v \\ \vartheta \end{bmatrix}_{\text{beam}} = \begin{bmatrix} 1 & 0 & -\Delta y \\ 0 & 1 & \Delta x \\ 0 & 0 & 1 \end{bmatrix} \begin{bmatrix} u \\ v \\ \vartheta \end{bmatrix}_{\text{mass}}, \tag{5.4}$$

with u, v and ϑ the x-displacement, the y-displacement and the rotation angle of a node, respectively, and where $\Delta x = x_{\text{beam}} - x_{\text{mass}}$ (same for Δy).

The shape of the drive beams is parametrized using a superimposition of five harmonics according to

$$y(x) = y_0(x) + \sum_{k=1}^{5} A_k \sin\left(\frac{k\pi}{L} x\right), \tag{5.5}$$

where L is the length of the beam, $y_0(x)$ represents the original y coordinates as if the beams were straight lines and A_k are the amplitudes of the harmonics. The other parameters of the optimization are the length and width of the drive beams (L_d and W_d), the length and width of the sense beams (L_s and W_s) and the width of the connecting elements between the sense beams W_c. As commonly done in MEMS devices [43], we impose a symmetry about the vertical axis, meaning that the two top drive beams, the two bottom drive beams and the two folded beams are symmetric. Therefore, the geometry of the MEMS gyroscope is defined by a total number of 16 parameters.

The optimization problem aims at imposing the frequencies ω_{drive} and ω_{sense} corresponding to the drive and sense mode shapes, respectively (figure 5). In addition, a point $(\Omega_{\text{drive}}, x_{\text{drive}})$ is imposed for the backbone curve associated with the drive mode. To this end, the optimization problem is stated as

$$\begin{aligned} \min_{\boldsymbol{\mu}} \quad & J, \\ \text{s.t.} \quad & \omega_{\text{drive}} - \omega_{\text{drive},0} = 0, \\ & \omega_{\text{sense}} - \omega_{\text{sense},0} = 0, \\ & \Omega_{\text{drive}}(\varrho(x_{\text{drive},0})) - \Omega_{\text{drive},0} = 0, \\ & \boldsymbol{\mu}_L \le \boldsymbol{\mu} \le \boldsymbol{\mu}_U, \end{aligned} \tag{5.6}$$

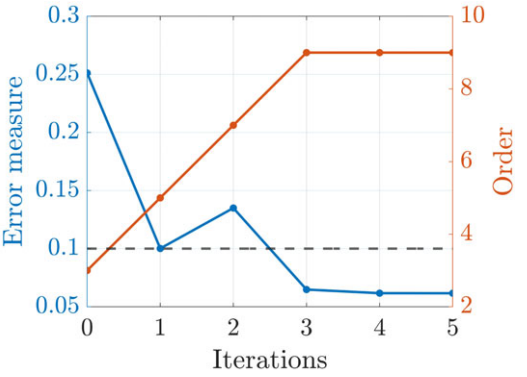

Figure 6. Evolution of the error measure ε and expansion order during the optimization of the MEMS gyroscope example.

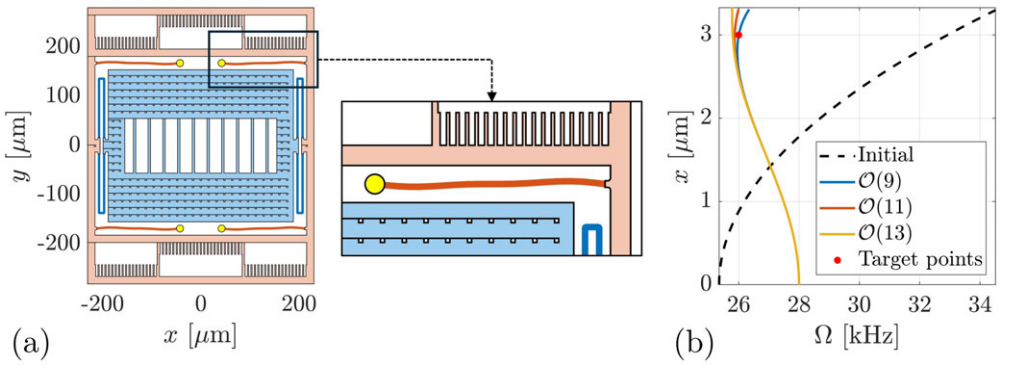

Figure 7. Solution of problem (5.6). (a) Optimal layout for the MEMS gyroscope. As can be seen in the inset, the drive beams are not straight anymore. (b) Backbone curve associated with the drive mode of the optimized layout (x is the RMS value of the drive frame y-displacement). Solutions at expansion orders 11 and 13 are reported for convergence analysis.

where the target values are $\omega_{\text{drive},0} = 28\,\text{kHz}$, $\omega_{\text{sense},0} = 26\,\text{kHz}$, $x_{\text{drive}},0 = 3\,\mu\text{m}$ and $\Omega_{\text{drive},0} = 26\,\text{kHz}$. The beam lengths are allowed to vary between $-25\,\mu\text{m}$ and $25\,\mu\text{m}$, while the beams widths between $-1\,\mu\text{m}$ and $1\,\mu\text{m}$. The drive beam amplitudes are bounded between $5\,\mu\text{m}$ and $-5\,\mu\text{m}$. At the first iteration, the design variables are all zero.

Using the adjoint method for the sensitivity of the frequencies ω_{drive}, ω_{sense} and Ω_{drive}, the optimization reaches convergence in five iterations (approx. 1 min and 5 s on a Windows workstation equipped with an Intel Core i9-13900KS CPU at 3.20 GHz and 128 GB of RAM at 4200 MT s^{-1}). During the optimization, the expansion order is automatically adjusted to keep the error measure [33] below a threshold of 10^{-1}. In particular, the expansion order has been increased from three to nine (figure 6).

The optimal layout is shown in figure 7a, while the backbone curve associated with the drive mode is computed using two expansion orders (figure 7b) to check the convergence of the SSM reduction.

(d) Topology optimization of an Messerschmitt–Bölkow–Blohm beam

We consider a topology optimization problem [25] to demonstrate the scalability and efficiency of the proposed method. Specifically, we examine the classical Messerschmitt–Bölkow–Blohm (MBB) beam configuration, illustrated in figure 9a. The black region denotes a fixed proof mass

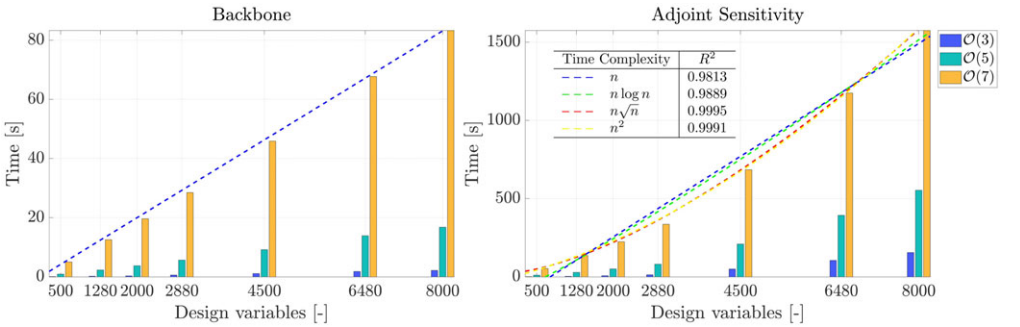

Figure 8. Computational times for evaluating the backbone curve (left) and its adjoint sensitivity (right) in a topology optimization problem, using different numbers of design variables (finite elements) and expansion orders. To estimate time complexity, the adjoint sensitivity timings (right) at the highest expansion order are fitted with four candidate scaling laws: (_) n, (_) $n \log n$, (_) $n\sqrt{n}$ and (_) n^2. For reference, computing the sensitivity using the direct differentiation approach for a system with 500 design variables and an $\mathcal{O}(3)$ SSM takes 83.5 s, nearly 70 times longer than the adjoint method.

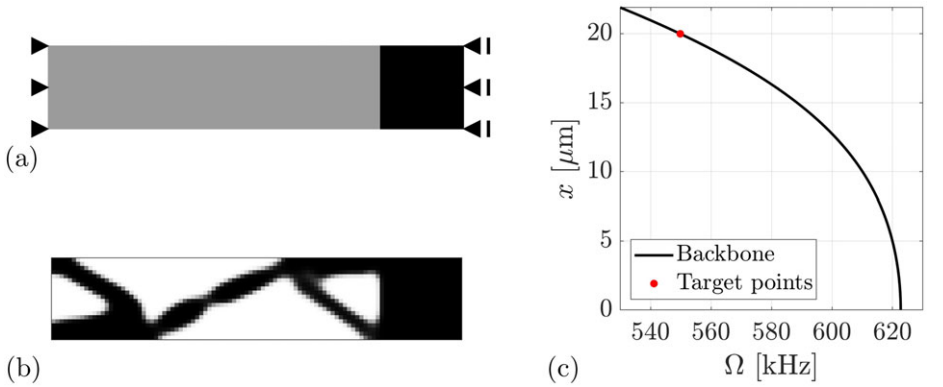

Figure 9. (a) Problem settings and initial conditions for the MBB beam, with a 100 × 20 finite element mesh (2000 design variables). (b) Optimal layout and (c) corresponding backbone curve obtained solving problem (5.7).

that remains unchanged throughout the optimization process. The left-hand edge of the domain is subjected to fixed boundary conditions, while the right-hand edge permits only horizontal displacements.

The material is modelled as polysilicon [43], characterized by a Young's modulus of $E = 148$ GPa, Poisson's ratio $\nu = 0.23$ and density $\varrho = 2330\,\mathrm{kg\,m^{-3}}$. A plane stress condition is assumed with a uniform out-of-plane thickness of 24 µm. The design domain, measuring 500 µm × 100 µm, is discretized into a 100 × 20 finite element mesh.

We adopt a standard density-based formulation for topology optimization [25], where each element is assigned a design variable $\mu \in [0, 1]$, representing its material density (0 for void, 1 for solid). These densities are used to interpolate material properties, specifically Young's modulus and density, using the solid isotropic material with penalization method [45]. See appendix H for all the details.

Before defining the optimization problem, we benchmark the routines by evaluating the backbone curve and its adjoint sensitivity for the MBB structure using different numbers of design variables (i.e. elements in the finite element grid) and expansion orders (figure 8). These timings, recorded on a Windows workstation equipped with an Intel Core i9-13900KS CPU at 3.20 GHz and 128 GB of RAM at 4200 MT s^{-1}, provide insights into the scalability of the proposed

approach for topology optimization. In this context, the number of degrees of freedom grows with the number of design variables, as each finite element is associated with a design variable. The backbone curve evaluation scales linearly with the number of design variables, while the adjoint sensitivity shows a complexity best approximated by $n\sqrt{n}$, as indicated by its R^2 value. Since backbone and sensitivity evaluations are the most time-consuming steps in the optimization loop [34], this benchmark also serves as a rough predictor of the iteration time.

The objective of this example is to maximize the eigenfrequency ω_y associated with the mode shape with the maximum displacement of the proof mass along the y direction. In addition, we prescribe the following target point on the backbone curve associated with the same mode:

$$(\Omega_{\text{target}}, x_{\text{target}}) = (550\,\text{kHz}, 20\,\mu\text{m}).$$

The corresponding optimization problem is defined as

$$\begin{aligned} \max_{\boldsymbol{\mu}} \quad & \omega_y, \\ \text{s.t.} \quad & (\Omega(\varrho(x_{\text{target}}))/\Omega_{\text{target}} - 1)^2 - \varepsilon^2 \leq 0, \\ & V - V_{\max} \leq 0, \\ & \mathbf{0} \leq \boldsymbol{\mu} \leq \mathbf{1}, \end{aligned} \tag{5.7}$$

where $V_{\max} = 50\%$ is used to limit the volume to the 50% of the total one, and $\epsilon = 10^{-3}$ is used to impose the frequency $\Omega(x_{\text{target}})$ to the target value within a tolerance of 0.1%.

Using a constant-order $\mathcal{O}(5)$ SSM reduction, the optimization converges after 98 iterations, requiring a total of 1 h, 31 min and 31 s. The average time per iteration is 56 s, which is in accordance with the benchmark in figure 8. The times are measured on a Windows workstation equipped with an Intel Core i9-13900KS CPU at 3.20 GHz and 128 GB of RAM at 4200 MT s^{-1}. The optimal layout and the corresponding backbone curve are shown in figure 9b,c. The solution is characterized by frequencies $\omega_y = 622.7$ kHz and $\Omega(x_{\text{target}}) = 549.8$ kHz. The relative difference between $\Omega(x_{\text{target}})$ and Ω_{target} is 0.03%, which is below the 0.1% tolerance.

6. Conclusion

This work presents an optimization framework for tailoring the nonlinear dynamic response of lightly damped mechanical systems by leveraging SSM reduction. The use of adjoint sensitivities in this formulation significantly reduces the computational cost compared to direct differentiation, allowing for the structural optimization of systems with a high number of design variables. By formulating the backbone curve and its sensitivity directly in the physical space, the proposed method enables optimization of the physical frequency–amplitude relation. The use of multi-index notation in our derivations overcomes the prior computational limitations of tensor-based formulation [33]. As our expressions enable optimization via SSMs up to arbitrary polynomial orders, we demonstrated how the optimization accuracy can be systematically controlled by automatic adjustment of the SSM expansion order.

We demonstrated the effectiveness and scalability of the proposed framework through several numerical examples, including the first application of topology optimization in nonlinear structural dynamics using arbitrary-order SSMs. This approach broadens the scope of SSM-based methods, making them viable for practical engineering applications that require precise control over nonlinear dynamic behaviour.

Future developments will focus on extending this approach to optimize forced-frequency responses, multiple modes with internal resonances and parametric amplification.

Data accessibility. This article does not contain any additional data.

Declaration of AI use. We have not used AI-assisted technologies in creating this article.

Authors' contributions. M.P.: conceptualization, formal analysis, investigation, methodology, software, validation, visualization, writing—original draft; J.M.: conceptualization, formal analysis, software, supervision,

validation, visualization, writing—review and editing; S.J.: validation, visualization, writing—review and editing; M.L.: validation, visualization, writing—review and editing; F.B.: funding acquisition, project administration, resources, supervision, writing—review and editing.

All authors gave final approval for publication and agreed to be held accountable for the work performed therein.

Conflict of interest declaration. We declare we have no competing interests.

Funding. The study was funded by STMicroelectronics (award no. 4000614871); National Natural Science Foundation of China (no. 12302014); State Key Laboratory of Structural Analysis, Optimization and CAE Software for Industrial Equipment (GZ24117).

Acknowledgements. M.P. acknowledges the financial support of STMicroelectronics. M.L. acknowledges the financial support of the National Natural Science Foundation of China and the State Key Laboratory of Structural Analysis, Optimization and CAE Software for Industrial Equipment.

Appendix A. On the Rayleigh damping coefficients

The SSM formulation described hereby holds for lightly damped mechanical systems for which $\xi < 1$. By looking at equation (2.12), this condition becomes

$$\alpha_R - 2\omega + \beta_R \omega^2 < 0, \tag{A 1}$$

where $\omega > 0$. However, the eigenfrequency ω may change during the optimization process, and we cannot strictly ensure that $\xi < 1$ if α_R and β_R are fixed. Assuming that $\alpha_R > 0$ and $\beta_R > 0$, and knowing that the roots of the equality associated to equation (A 1) are

$$\omega_{1,2} = \frac{1 \pm \sqrt{1 - \alpha_R \beta_R}}{\beta_R}, \tag{A 2}$$

we have the following conditions on ω to satisfy equation (A 1):

$$\begin{cases} \text{if} \quad \beta_R = 0 & \rightarrow \omega > \dfrac{\alpha_R}{2}, \\ \text{if} \quad \alpha_R = 0 & \rightarrow \omega < \dfrac{2}{\beta_R}, \\ \text{if} \quad 0 < \alpha_R \beta_R < 1 & \rightarrow \omega_1 < \omega < \omega_2, \\ \text{if} \quad \alpha_R \beta_R > 1 & \rightarrow \text{equation (A 1) is never satisfied (i.e. } \xi > 1). \end{cases} \tag{A 3}$$

In this work, α_R and β_R are selected and fixed before starting the optimization routine, so their values should be carefully chosen according to the conditions above, depending on the specific problem at hand.

A possible alternative is to impose the value of ξ and compute α_R and β_R accordingly [35].

Appendix B. Multi-index notation

A multi-index $\boldsymbol{m} \in \mathbb{N}^M$ of order $m = |\boldsymbol{m}|_1$ is an M-dimensional vector for which addition, subtraction and other operations are defined element-wise. For instance, the multi-indices can be used to define multivariate monomials of order m as

$$\boldsymbol{p}^{\boldsymbol{m}} = p_1^{m_1} \cdots p_M^{m_M}. \tag{B 1}$$

To denote quantities related to a specific multi-index $\boldsymbol{m} = \{x, y\}$, we use the subscript $\bullet_{xy}$. For instance, the manifold coefficient related to $\boldsymbol{m} = \{2, 1\}$ is $\boldsymbol{w}_{21}$.

In addition, given a multi-index $\boldsymbol{m} = \{x, y\}$, define the symmetric multi-index $\boldsymbol{m}^s = \{y, x\}$.

Appendix C. Near-resonance condition

With $\boldsymbol{\Lambda} = \{\lambda_1, \lambda_2\}^T = \{\lambda, \bar{\lambda}\}^T$, we have

$$\Lambda_{\boldsymbol{m}} = \boldsymbol{\Lambda} \cdot \boldsymbol{m} = m_1\lambda + m_2\bar{\lambda} = -(m_1 + m_2)\alpha + \mathrm{i}(m_1 - m_2)\omega_d. \tag{C 1}$$

For an *undamped* system ($\xi = 0$), we have

$$\mathrm{Re}(\lambda) = \mathrm{Re}(\bar{\lambda}) = 0 \implies \Lambda_{\boldsymbol{m}} = \mathrm{i}(m_1 - m_2)\omega.$$

In this case, an *inner* resonance occurs if

$$\left.\begin{aligned} \Lambda_{\boldsymbol{m}} &= \lambda_j, \quad j = 1, 2, \\ \mathrm{i}(m_1 - m_2)\omega &= \pm\mathrm{i}\omega \\ \text{and} \qquad m_1 - m_2 &= \pm 1. \end{aligned}\right\} \tag{C 2}$$

As a consequence, we can conclude that at the *even* order m there are no inner resonances and the coefficients $\boldsymbol{R}_{\boldsymbol{m}}$ are null, whereas at the *odd* order m there are only two multi-indices such that

$$\left.\begin{aligned} m_1 - m_2 = +1 &\implies R^1_{\boldsymbol{m}} \neq 0 \\ \text{and} \qquad m_1 - m_2 = -1 &\implies R^2_{\boldsymbol{m}} \neq 0. \end{aligned}\right\} \tag{C 3}$$

For a generic damped system instead, we write

$$-(m_1 + m_2)\alpha + \mathrm{i}(m_1 - m_2)\omega_d = -\alpha \pm \mathrm{i}\omega_d, \tag{C 4}$$

resulting in the following conditions:

$$\left.\begin{aligned} m_1 - m_2 &= \pm 1 \\ \text{and} \qquad m_1 + m_2 &= 1. \end{aligned}\right\} \tag{C 5}$$

To strictly satisfy the above expressions, the only possible solutions are $\boldsymbol{m} = \{1, 0\}$ and $\boldsymbol{m} = \{0, 1\}$. However, under the assumption that $|\mathrm{Re}\,\lambda| \ll |\mathrm{Im}\lambda|$, we can safely ignore the second constraint in equation (C 2) and use the *near-resonance* condition $\Lambda_{\boldsymbol{m}} \approx \lambda_j$.

Appendix D. SSM computation

(a) Leading order

At the leading order, there are two multi-indices $\boldsymbol{m} = \{1, 0\}$ and $\boldsymbol{m} = \{0, 1\}$. The coefficients for the nonlinear dynamics are typically chosen as the eigenvalues of the system:

$$R^1_{10} = \lambda_1 \quad \text{and} \quad R^2_{01} = \lambda_2, \tag{D 1}$$

while $R^2_{10} = R^1_{01} = 0$. The manifold coefficients are then selected as

$$\boldsymbol{w}_{10} = \boldsymbol{\varphi}, \quad \boldsymbol{w}_{01} = \boldsymbol{\varphi}, \quad \dot{\boldsymbol{w}}_{10} = \lambda_1\boldsymbol{\varphi}, \quad \dot{\boldsymbol{w}}_{01} = \lambda_2\boldsymbol{\varphi}. \tag{D 2}$$

(b) Higher orders

After choosing the leading-order coefficients, the higher-order ones are computed iteratively, starting with the lowest one. The first step is to compute the eigenvalue coefficient:

$$\Lambda_{\boldsymbol{m}} = \boldsymbol{m} \cdot \boldsymbol{\Lambda}. \tag{D 3}$$

Then, using tensor notation, the nonlinear force contribution at the current order is

$$f^i_{\boldsymbol{m}} = \sum_{\substack{\boldsymbol{u},\boldsymbol{k}\in\mathbb{N}^2 \\ \boldsymbol{u}+\boldsymbol{k}=\boldsymbol{m}}} T^{ijk}_2 w^j_{\boldsymbol{u}} w^k_{\boldsymbol{k}} + \sum_{\substack{\boldsymbol{u},\boldsymbol{k},\boldsymbol{l}\in\mathbb{N}^2 \\ \boldsymbol{u}+\boldsymbol{k}+\boldsymbol{l}=\boldsymbol{m}}} T^{ijkl}_3 w^j_{\boldsymbol{u}} w^k_{\boldsymbol{k}} w^l_{\boldsymbol{l}}. \tag{D 4}$$

The vectors $\boldsymbol{V}_m$ and $\dot{\boldsymbol{V}}_m$ collect the contributions from the orders lower than the current one. These vectors are computed as

$$\boldsymbol{V}_m = \sum_{j=1}^{2} \sum_{\substack{\boldsymbol{u},\boldsymbol{k}\in\mathbb{N}^2 \\ 1<u,k<m \\ \boldsymbol{u}+\boldsymbol{k}-\boldsymbol{e}_j=\boldsymbol{m}}} w_{\boldsymbol{u}} u_j R_{\boldsymbol{k}}^j \quad \text{and} \quad \dot{\boldsymbol{V}}_m = \sum_{j=1}^{2} \sum_{\substack{\boldsymbol{u},\boldsymbol{k}\in\mathbb{N}^2 \\ 1<u,k<m \\ \boldsymbol{u}+\boldsymbol{k}-\boldsymbol{e}_j=\boldsymbol{m}}} \dot{w}_{\boldsymbol{u}} u_j R_{\boldsymbol{k}}^j. \tag{D 5}$$

The vectors $\boldsymbol{f}_m$, $\boldsymbol{V}_m$, and $\dot{\boldsymbol{V}}_m$ are then combined into

$$\boldsymbol{C}_m = -\mathbf{M}\dot{\boldsymbol{V}}_m - (\Lambda_m \mathbf{M} + \mathbf{C})\boldsymbol{V}_m - \boldsymbol{f}_m. \tag{D 6}$$

For multi-indices that are in a near-resonance condition (appendix C), the vector $\boldsymbol{C}_m$ is used in the computation of the reduced dynamics coefficient:

$$R_m^j = \frac{\boldsymbol{\varphi}^T \boldsymbol{C}_m}{\Lambda_m + \lambda_j + \alpha_R + \beta_R \omega^2}. \tag{D 7}$$

Next, the left-hand side of the cohomological equation is assembled as

$$\mathbf{L}_m = \mathbf{K} + \Lambda_m \mathbf{C} + \Lambda_m^2 \mathbf{M}, \tag{D 8}$$

while the right-hand side reads

$$\boldsymbol{h}_m = \boldsymbol{C}_m + \sum_{j=1}^{2} \boldsymbol{D}_m^j R_m^j, \tag{D 9}$$

where

$$\boldsymbol{D}_m^j = -[(\Lambda_m + \lambda_j)\mathbf{M} + \mathbf{C}]\boldsymbol{\varphi}. \tag{D 10}$$

Notice that $\boldsymbol{D}_m^j$ is required only if $R_m^j \neq 0$ (near-resonance condition).

The cohomological equation is solved for the manifold coefficient $\boldsymbol{w}_m$:

$$\mathbf{L}_m \boldsymbol{w}_m = \boldsymbol{h}_m. \tag{D 11}$$

Finally, the manifold velocity coefficient is computed as

$$\dot{\boldsymbol{w}}_m = \Lambda_m \boldsymbol{w}_m + \sum_{j=1}^{2} R_m^j \boldsymbol{\varphi} + \boldsymbol{V}_m. \tag{D 12}$$

Property *(Symmetric multi-index)*. In a general setting, all these steps need to be repeated for every multi-index at each order. However, for the type of problem under consideration, the coefficients associated with symmetric multi-indices are complex conjugate (e.g. $\boldsymbol{w}_{12} = \bar{\boldsymbol{w}}_{21}$). This property applies to all coefficients involved in the SSM computation and is leveraged to reduce the overall computational cost. Specifically, we only need to compute the coefficients corresponding to multi-indices $\boldsymbol{m} = \{x, y\}$ satisfying $x \geq y$. Then, the coefficients for the remaining multi-indices, where $x < y$, are obtained as the complex conjugates of their symmetric counterparts.

Appendix E. Direct differentiation sensitivity

Using the chain rule, the derivative of the response frequency Ω (equation (3.10)) with respect to the design variable μ is

$$\frac{\mathrm{d}\Omega}{\mathrm{d}\mu} = \frac{1}{2}\mathrm{i}\left(\frac{\mathrm{d}\lambda_2}{\mathrm{d}\mu} - \frac{\mathrm{d}\lambda_1}{\mathrm{d}\mu}\right) + \frac{1}{2}\mathrm{i}\sum_{m>1}\left[\left(\frac{\mathrm{d}R_m^2}{\mathrm{d}\mu} - \frac{\mathrm{d}R_m^1}{\mathrm{d}\mu}\right)\varrho^{m-1} + \frac{\mathrm{d}\varrho}{\mathrm{d}\mu}(R_m^2 - R_m^1)(m-1)\varrho^{m-2}\right]. \tag{E 1}$$

The derivative of the reduced amplitude ϱ with respect to μ is computed by differentiating equation (3.13):

$$\frac{\mathrm{d}\varrho}{\mathrm{d}\mu} = -\frac{\sum_k x_k^i \sum_m \frac{\mathrm{d}w_m^i}{\mathrm{d}\mu} \boldsymbol{p}_k^m}{\sum_k x_k^i \sum_m w_m^i m \varrho^{m-1} \tilde{\boldsymbol{p}}_k^m}, \tag{E 2}$$

where $x_k^i = x^i(\vartheta_k)$, $\boldsymbol{p}_k = \boldsymbol{p}(\vartheta_k)$ and $\tilde{\boldsymbol{p}}_k = \{e^{\mathrm{i}\vartheta_k}, e^{-\mathrm{i}\vartheta_k}\}^T$.

To evaluate the sensitivity of Ω, the derivatives of λ, R_m^j and $\boldsymbol{w}_m$ are required. Before computing them, we need to evaluate the derivatives of ω and $\boldsymbol{\varphi}$ with respect to μ. These are computed together by differentiating the generalized eigenvalue problem (equation (2.10)) and the mass normalization condition (equation (2.11)):

$$\begin{bmatrix} \mathbf{K}-\omega^2\mathbf{M} & -2\omega\mathbf{M}\boldsymbol{\varphi} \\ -2\omega\boldsymbol{\varphi}^T\mathbf{M} & 0 \end{bmatrix} \begin{bmatrix} \frac{\mathrm{d}\boldsymbol{\varphi}}{\mathrm{d}\mu} \\ \frac{\mathrm{d}\omega}{\mathrm{d}\mu} \end{bmatrix} = \begin{bmatrix} \left(\omega^2\frac{\mathrm{d}\mathbf{M}}{\mathrm{d}\mu}-\frac{\mathrm{d}\mathbf{K}}{\mathrm{d}\mu}\right)\boldsymbol{\varphi} \\ \omega\boldsymbol{\varphi}^T\frac{\mathrm{d}\mathbf{M}}{\mathrm{d}\mu}\boldsymbol{\varphi} \end{bmatrix}. \tag{E 3}$$

Then, the derivative of the eigenvalue λ is computed as

$$\frac{\mathrm{d}\lambda}{\mathrm{d}\mu} = -\xi\frac{\mathrm{d}\omega}{\mathrm{d}\mu} - \omega\frac{\mathrm{d}\xi}{\mathrm{d}\mu} + \mathrm{i}\frac{\mathrm{d}\omega}{\mathrm{d}\mu}\sqrt{1-\xi^2} - \mathrm{i}\omega\frac{\xi}{\sqrt{1-\xi^2}}\frac{\mathrm{d}\xi}{\mathrm{d}\mu}, \tag{E 4}$$

where the derivative of the damping ratio ξ is

$$\frac{\mathrm{d}\xi}{\mathrm{d}\mu} = \frac{\beta_R\omega^2-\alpha_R}{2\omega^2}\frac{\mathrm{d}\omega}{\mathrm{d}\mu}. \tag{E 5}$$

Next, the derivatives of the leading-order SSM coefficients are

$$\frac{\mathrm{d}R_{10}^1}{\mathrm{d}\mu} = \frac{\mathrm{d}\bar{R}_{01}^2}{\mathrm{d}\mu} = \frac{\mathrm{d}\lambda}{\mathrm{d}\mu}, \quad \frac{\mathrm{d}\boldsymbol{w}_{10}}{\mathrm{d}\mu} = \frac{\mathrm{d}\bar{\boldsymbol{w}}_{01}}{\mathrm{d}\mu} = \frac{\mathrm{d}\boldsymbol{\varphi}}{\mathrm{d}\mu}, \quad \frac{\mathrm{d}\dot{\boldsymbol{w}}_{10}}{\mathrm{d}\mu} = \frac{\mathrm{d}\dot{\bar{\boldsymbol{w}}}_{01}}{\mathrm{d}\mu} = \frac{\mathrm{d}\lambda}{\mathrm{d}\mu}\boldsymbol{\varphi} + \lambda\frac{\mathrm{d}\boldsymbol{\varphi}}{\mathrm{d}\mu}. \tag{E 6}$$

After that, we can differentiate all the higher-order SSM coefficients starting from the lowest one. In particular, the derivative of the eigenvalue coefficient is simply

$$\frac{\mathrm{d}\Lambda_{\boldsymbol{m}}}{\mathrm{d}\mu} = \boldsymbol{m}\cdot\frac{\mathrm{d}\boldsymbol{\Lambda}}{\mathrm{d}\mu}. \tag{E 7}$$

Using tensor notation, it is possible to write the derivative of the nonlinear force contribution:

$$\begin{aligned}\frac{\mathrm{d}f_{\boldsymbol{m}}^i}{\mathrm{d}\mu} = &\sum_{\substack{\boldsymbol{u},\boldsymbol{k}\in\mathbb{N}^2 \\ \boldsymbol{u}+\boldsymbol{k}=\boldsymbol{m}}} \left[\frac{\mathrm{d}T_2^{ijk}}{\mathrm{d}\mu}w_{\boldsymbol{u}}^j w_{\boldsymbol{k}}^k + T_2^{ijk}\left(\frac{\mathrm{d}w_{\boldsymbol{u}}^j}{\mathrm{d}\mu}w_{\boldsymbol{k}}^k + w_{\boldsymbol{u}}^j\frac{\mathrm{d}w_{\boldsymbol{k}}^k}{\mathrm{d}\mu}\right)\right] \\ &+ \sum_{\substack{\boldsymbol{u},\boldsymbol{k},\boldsymbol{l}\in\mathbb{N}^2 \\ \boldsymbol{u}+\boldsymbol{k}+\boldsymbol{l}=\boldsymbol{m}}} \left[\frac{\mathrm{d}T_3^{ijkl}}{\mathrm{d}\mu}w_{\boldsymbol{u}}^j w_{\boldsymbol{k}}^k w_{\boldsymbol{l}}^l + T_3^{ijkl}\left(\frac{\mathrm{d}w_{\boldsymbol{u}}^j}{\mathrm{d}\mu}w_{\boldsymbol{k}}^k w_{\boldsymbol{l}}^l + w_{\boldsymbol{u}}^j\frac{\mathrm{d}w_{\boldsymbol{k}}^k}{\mathrm{d}\mu}w_{\boldsymbol{l}}^l + w_{\boldsymbol{u}}^j w_{\boldsymbol{k}}^k\frac{\mathrm{d}w_{\boldsymbol{l}}^l}{\mathrm{d}\mu}\right)\right].\end{aligned} \tag{E 8}$$

The derivatives of vectors $\boldsymbol{V}_{\boldsymbol{m}}$ and $\dot{\boldsymbol{V}}_{\boldsymbol{m}}$ are written as

$$\frac{\mathrm{d}\boldsymbol{V}_{\boldsymbol{m}}}{\mathrm{d}\mu} = \sum_{j=1}^{2}\sum_{\substack{\boldsymbol{u},\boldsymbol{k}\in\mathbb{N}^2 \\ 1<u,k<m \\ \boldsymbol{u}+\boldsymbol{k}-\boldsymbol{e}_j=\boldsymbol{m}}} u_j\left(\frac{\mathrm{d}\boldsymbol{w}_{\boldsymbol{u}}}{\mathrm{d}\mu}R_{\boldsymbol{k}}^j + \boldsymbol{w}_{\boldsymbol{u}}\frac{\mathrm{d}R_{\boldsymbol{k}}^j}{\mathrm{d}\mu}\right) \tag{E 9}$$

and

$$\frac{\mathrm{d}\dot{\boldsymbol{V}}_{\boldsymbol{m}}}{\mathrm{d}\mu} = \sum_{j=1}^{2}\sum_{\substack{\boldsymbol{u},\boldsymbol{k}\in\mathbb{N}^2 \\ 1<u,k<m \\ \boldsymbol{u}+\boldsymbol{k}-\boldsymbol{e}_j=\boldsymbol{m}}} u_j\left(\frac{\mathrm{d}\dot{\boldsymbol{w}}_{\boldsymbol{u}}}{\mathrm{d}\mu}R_{\boldsymbol{k}}^j + \dot{\boldsymbol{w}}_{\boldsymbol{u}}\frac{\mathrm{d}R_{\boldsymbol{k}}^j}{\mathrm{d}\mu}\right). \tag{E 10}$$

The derivative of vector $\boldsymbol{C}_{\boldsymbol{m}}$ reads

$$\frac{\mathrm{d}\boldsymbol{C}_{\boldsymbol{m}}}{\mathrm{d}\mu} = -\frac{\mathrm{d}\mathbf{M}}{\mathrm{d}\mu}\dot{\boldsymbol{V}}_{\boldsymbol{m}} - \mathbf{M}\frac{\mathrm{d}\dot{\boldsymbol{V}}_{\boldsymbol{m}}}{\mathrm{d}\mu} - (\Lambda_{\boldsymbol{m}}\mathbf{M}+\mathbf{C})\frac{\mathrm{d}\boldsymbol{V}_{\boldsymbol{m}}}{\mathrm{d}\mu} - \left(\frac{\mathrm{d}\Lambda_{\boldsymbol{m}}}{\mathrm{d}\mu}\mathbf{M} + \Lambda_{\boldsymbol{m}}\frac{\mathrm{d}\mathbf{M}}{\mathrm{d}\mu} + \frac{\mathrm{d}\mathbf{C}}{\mathrm{d}\mu}\right)\boldsymbol{V}_{\boldsymbol{m}} - \frac{\mathrm{d}\boldsymbol{f}_{\boldsymbol{m}}}{\mathrm{d}\mu}. \tag{E 11}$$

For the multi-indices that are in near-resonance condition (appendix C), we also need to differentiate the reduced dynamics coefficient:

$$\frac{\mathrm{d}R_m^j}{\mathrm{d}\mu} = \frac{\frac{\mathrm{d}\boldsymbol{\varphi}^T}{\mathrm{d}\mu}\boldsymbol{C}_m + \boldsymbol{\varphi}^T\frac{\mathrm{d}\mathbf{C}_m}{\mathrm{d}\mu}}{\Lambda_m + \lambda_j + \alpha_R + \beta_R\omega^2} - R_m^j\frac{\frac{\mathrm{d}\Lambda_m}{\mathrm{d}\mu} + \frac{\mathrm{d}\lambda_j}{\mathrm{d}\mu} + 2\beta_R\omega\frac{\mathrm{d}\omega}{\mathrm{d}\mu}}{\Lambda_m + \lambda_j + \alpha_R + \beta_R\omega^2}. \tag{E 12}$$

Next, the derivative of the manifold coefficient is obtained by differentiating the cohomological equation:

$$\mathbf{L}_m\frac{\mathrm{d}\boldsymbol{w}_m}{\mathrm{d}\mu} = \frac{\mathrm{d}\boldsymbol{h}_m}{\mathrm{d}\mu} - \frac{\mathrm{d}\mathbf{L}_m}{\mathrm{d}\mu}\boldsymbol{w}_m, \tag{E 13}$$

where

$$\frac{\mathrm{d}\mathbf{L}_m}{\mathrm{d}\mu} = \frac{\mathrm{d}\mathbf{K}}{\mathrm{d}\mu} + \Lambda_m\frac{\mathrm{d}\mathbf{C}}{\mathrm{d}\mu} + \Lambda_m^2\frac{\mathrm{d}\mathbf{M}}{\mathrm{d}\mu} + (\mathbf{C} + 2\Lambda_m\mathbf{M})\frac{\mathrm{d}\Lambda_m}{\mathrm{d}\mu} \tag{E 14}$$

$$\frac{\mathrm{d}\boldsymbol{h}_m}{\mathrm{d}\mu} = \frac{\mathrm{d}\boldsymbol{C}_m}{\mathrm{d}\mu} + \sum_{j=1}^{2}\left(\frac{\mathrm{d}\boldsymbol{D}_m^j}{\mathrm{d}\mu}R_m^j + \boldsymbol{D}_m^j\frac{\mathrm{d}R_m^j}{\mathrm{d}\mu}\right) \tag{E 15}$$

and

$$\frac{\mathrm{d}\boldsymbol{D}_m^j}{\mathrm{d}\mu} = -[(\Lambda_m + \lambda_j)\mathbf{M} + \mathbf{C}]\frac{\mathrm{d}\boldsymbol{\varphi}}{\mathrm{d}\mu} - \left[\left(\frac{\mathrm{d}\Lambda_m}{\mathrm{d}\mu} + \frac{\mathrm{d}\lambda_j}{\mathrm{d}\mu}\right)\mathbf{M} + (\Lambda_m + \lambda_j)\frac{\mathrm{d}\mathbf{M}}{\mathrm{d}\mu} + \frac{\mathrm{d}\mathbf{C}}{\mathrm{d}\mu}\right]\boldsymbol{\varphi}. \tag{E 16}$$

Finally, the derivative of the manifold velocity coefficient is

$$\frac{\mathrm{d}\dot{\boldsymbol{w}}_m}{\mathrm{d}\mu} = \frac{\mathrm{d}\Lambda_m}{\mathrm{d}\mu}\boldsymbol{w}_m + \Lambda_m\frac{\mathrm{d}\boldsymbol{w}_m}{\mathrm{d}\mu} + \frac{\mathrm{d}\boldsymbol{V}_m}{\mathrm{d}\mu} + \sum_{j=1}^{2}\left(\frac{\mathrm{d}R_m^j}{\mathrm{d}\mu}\boldsymbol{\varphi} + R_m^j\frac{\mathrm{d}\boldsymbol{\varphi}}{\mathrm{d}\mu}\right). \tag{E 17}$$

Appendix F. Adjoint sensitivity of the damped frequency

Using the adjoint method, and assuming mass normalized mode shapes (equation (2.11)), the sensitivity of the eigenfrequency ω with respect to the design variable μ is

$$\frac{\mathrm{d}\omega}{\mathrm{d}\mu} = \frac{\boldsymbol{\varphi}^T\left(\frac{\partial\mathbf{K}}{\partial\mu} - \omega^2\frac{\partial\mathbf{M}}{\partial\mu}\right)\boldsymbol{\varphi}}{2\omega}. \tag{F 1}$$

Using this expression, it is possible to write the sensitivity of the damped frequency ω_d as

$$\frac{\mathrm{d}\omega_d}{\mathrm{d}\mu} = \frac{\mathrm{d}\omega}{\mathrm{d}\mu}\sqrt{1-\xi^2} - \omega\frac{\xi}{\sqrt{1-\xi^2}}\frac{\mathrm{d}\xi}{\mathrm{d}\mu}, \tag{F 2}$$

where the derivative of the damping ratio ξ is

$$\frac{\mathrm{d}\xi}{\mathrm{d}\mu} = \frac{\beta_R\omega^2 - \alpha_R}{2\omega^2}\frac{\mathrm{d}\omega}{\mathrm{d}\mu}. \tag{F 3}$$

Appendix G. Partial derivatives

(a) Partial derivatives with respect to the reduced amplitude

The partial derivative of the response frequency Ω with respect to the reduced amplitude ϱ is

$$\frac{\partial\Omega}{\partial\varrho} = \frac{1}{2}\mathrm{i}\sum_{m>1}(R_{\boldsymbol{m}}^2 - R_{\boldsymbol{m}}^1)(m-1)\varrho^{m-2}. \tag{G 1}$$

The partial derivative of the RMS physical amplitude x with respect to the reduced amplitude ϱ is

$$\frac{\partial x}{\partial\varrho} = \frac{1}{N_\vartheta x}\sum_k x_k^i\sum_{\boldsymbol{m}} w_{\boldsymbol{m}}^i m\varrho^{m-1}\tilde{\boldsymbol{p}}_k^{\boldsymbol{m}}, \tag{G 2}$$

where $x_k^i = x^i(\vartheta_k)$ and $\tilde{\boldsymbol{p}}_k = \{e^{\mathrm{i}\vartheta_k}, e^{-\mathrm{i}\vartheta_k}\}^T$.

(b) Partial derivatives with respect to the manifold coefficients

Before deep diving into the partial derivatives, it is important to highlight that quantities at a given order do not depend on the manifold coefficients at higher orders. Therefore, the partial derivative of a term at order q with respect to the manifold coefficient at order m is non-zero only if $q > m$.

Using tensor notation, the partial derivative of the nonlinear force contribution is

$$\frac{\partial f_q^i}{\partial w_m^p} = \sum_{\substack{u,k\in\mathbb{N}^2 \\ u+k=q}} T_2^{ijk}\left(\frac{\partial w_u^j}{\partial w_m^p} w_k^k + w_u^j \frac{\partial w_k^k}{\partial w_m^p}\right) + \sum_{\substack{u,k,l\in\mathbb{N}^2 \\ u+k+l=q}} T_3^{ijkl}\left(\frac{\partial w_u^j}{\partial w_m^p} w_k^k w_l^l + w_u^j \frac{\partial w_k^k}{\partial w_m^p} w_l^l + w_u^j w_k^k \frac{\partial w_l^l}{\partial w_m^p}\right), \tag{G 3}$$

where

$$\frac{\partial w_u^j}{\partial w_m^p} = \begin{cases} 1 & \text{if } \boldsymbol{u} = \boldsymbol{m} \quad \text{and} \quad p = j, \\ 0 & \text{otherwise.} \end{cases} \tag{G 4}$$

The same condition applies to all the other partial derivatives in equation (G 3).

The partial derivative $\frac{\partial f_q}{\partial w_m}$ is a matrix which, in general, can be dense. Therefore, to avoid storing the full matrix, the product $\boldsymbol{v}^T \frac{\partial f_q}{\partial w_m}$ is stored instead, where $\boldsymbol{v}$ represents a vector that multiplies $\boldsymbol{f}_q$ in the Lagrangian function.

The partial derivative of vectors $\boldsymbol{V}_q$ and $\dot{\boldsymbol{V}}_q$ are

$$\boldsymbol{v}^T \frac{\partial \boldsymbol{V}_q}{\partial \boldsymbol{w}_m} = \sum_{j=1}^{2} \sum_{\substack{u,k\in\mathbb{N}^2 \\ 1<u,k<q \\ u+k-e_j=q}} u_j \left(\boldsymbol{v}^T \frac{\partial \boldsymbol{w}_u}{\partial \boldsymbol{w}_m} R_k^j + (\boldsymbol{v}^T \boldsymbol{w}_u) \frac{\partial R_k^j}{\partial \boldsymbol{w}_m}\right) \tag{G 5}$$

and

$$\boldsymbol{v}^T \frac{\partial \dot{\boldsymbol{V}}_q}{\partial \boldsymbol{w}_m} = \sum_{j=1}^{2} \sum_{\substack{u,k\in\mathbb{N}^2 \\ 1<u,k<q \\ u+k-e_j=q}} u_j \left(\boldsymbol{v}^T \frac{\partial \dot{\boldsymbol{w}}_u}{\partial \boldsymbol{w}_m} R_k^j + (\boldsymbol{v}^T \dot{\boldsymbol{w}}_u) \frac{\partial R_k^j}{\partial \boldsymbol{w}_m}\right), \tag{G 6}$$

where the products $\boldsymbol{v}^T \boldsymbol{w}_u$ and $\boldsymbol{v}^T \dot{\boldsymbol{w}}_u$ are scalar quantities. Moreover, the product $\boldsymbol{v}^T \frac{\partial \boldsymbol{w}_u}{\partial \boldsymbol{w}_m}$ is equal to $\boldsymbol{v}^T$ if $\boldsymbol{u} = \boldsymbol{m}$, otherwise it is equal to a null row vector.

The partial derivative of vector $\boldsymbol{C}_q$ is

$$\boldsymbol{v}^T \frac{\partial \boldsymbol{C}_q}{\partial \boldsymbol{w}_m} = -\boldsymbol{v}^T \mathbf{M} \frac{\partial \dot{\boldsymbol{V}}_q}{\partial \boldsymbol{w}_m} - \boldsymbol{v}^T \frac{\partial \boldsymbol{f}_q}{\partial \boldsymbol{w}_m} - \boldsymbol{v}^T (\Lambda_q \mathbf{M} + \mathbf{C}) \frac{\partial \boldsymbol{V}_q}{\partial \boldsymbol{w}_m}. \tag{G 7}$$

The partial derivative of the reduced dynamics coefficient is

$$\frac{\partial R_q^j}{\partial \boldsymbol{w}_m} = \frac{\boldsymbol{\varphi}^T \frac{\partial \boldsymbol{C}_q}{\partial \boldsymbol{w}_m}}{\Lambda_q + \lambda_j + \alpha_R + \beta_R \omega^2}, \tag{G 8}$$

where $\boldsymbol{\varphi}^T \frac{\partial \boldsymbol{C}_q}{\partial \boldsymbol{w}_m}$ is computed using equation (G 7) by setting $\boldsymbol{v} = \boldsymbol{\varphi}$.

The partial derivative of the right-hand side of the cohomological equation is

$$\boldsymbol{v}^T \frac{\partial \boldsymbol{h}_q}{\partial \boldsymbol{w}_m} = -\boldsymbol{v}^T \frac{\partial \boldsymbol{C}_q}{\partial \boldsymbol{w}_m} - \sum_{j=1}^{2} (\boldsymbol{v}^T \boldsymbol{D}_q^j) \frac{\partial R_q^j}{\partial \boldsymbol{w}_m}, \tag{G 9}$$

where the product $\boldsymbol{v}^T \boldsymbol{D}_q^j$ is a scalar quantity, and the vector $\boldsymbol{D}_q^j$ does not depend on the manifold coefficients.

The partial derivative of the manifold velocity coefficient is

$$\boldsymbol{v}^T \frac{\partial \dot{\boldsymbol{w}}_{\boldsymbol{q}}}{\partial \boldsymbol{w}_{\boldsymbol{m}}} = \Lambda_q \boldsymbol{v}^T \frac{\partial \boldsymbol{w}_{\boldsymbol{q}}}{\partial \boldsymbol{w}_{\boldsymbol{m}}} + (\boldsymbol{v}^T \boldsymbol{\varphi}) \sum_{j=1}^{2} \frac{\partial R_{\boldsymbol{q}}^j}{\partial \boldsymbol{w}_{\boldsymbol{m}}} + \boldsymbol{v}^T \frac{\partial \boldsymbol{V}_{\boldsymbol{q}}}{\partial \boldsymbol{w}_{\boldsymbol{m}}}, \tag{G 10}$$

where the product $\boldsymbol{v}^T \boldsymbol{\varphi}$ is a scalar quantity.

The partial derivative of the physical amplitude is

$$\frac{\partial x}{\partial \boldsymbol{w}_{\boldsymbol{m}}} = \frac{1}{N_\vartheta x} \sum_k x_k^i \boldsymbol{a}^T \boldsymbol{p}_k^{\boldsymbol{m}}, \tag{G 11}$$

where $\boldsymbol{a}$ is a vector such that $a_j = 1$ if $i = j$, 0 otherwise.

The partial derivative of the response frequency is

$$\frac{\partial \Omega}{\partial \boldsymbol{w}_{\boldsymbol{m}}} = \frac{1}{2} \mathrm{i} \sum_{q>m} \left(\frac{\partial R_{\boldsymbol{q}}^2}{\partial \boldsymbol{w}_{\boldsymbol{m}}} - \frac{\partial R_{\boldsymbol{q}}^1}{\partial \boldsymbol{w}_{\boldsymbol{m}}} \right) \varrho^{q-1}. \tag{G 12}$$

(c) Partial derivatives with respect to the mode shape

Using tensor notation, the partial derivative of the nonlinear force contribution is

$$\frac{\partial f_{\boldsymbol{m}}^i}{\partial \varphi^p} = \sum_{\substack{\boldsymbol{u},\boldsymbol{k} \in \mathbb{N}^2 \\ \boldsymbol{u}+\boldsymbol{k}=\boldsymbol{m}}} T_2^{ijk} \left(\frac{\partial w_{\boldsymbol{u}}^j}{\partial \varphi^p} w_{\boldsymbol{k}}^k + w_{\boldsymbol{u}}^j \frac{\partial w_{\boldsymbol{k}}^k}{\partial \varphi^p} \right) + \sum_{\substack{\boldsymbol{u},\boldsymbol{k},\boldsymbol{l} \in \mathbb{N}^2 \\ \boldsymbol{u}+\boldsymbol{k}+\boldsymbol{l}=\boldsymbol{m}}} T_3^{ijkl} \left(\frac{\partial w_{\boldsymbol{u}}^j}{\partial \varphi^p} w_{\boldsymbol{k}}^k w_{\boldsymbol{l}}^l + w_{\boldsymbol{u}}^j \frac{\partial w_{\boldsymbol{k}}^k}{\partial \varphi^p} w_{\boldsymbol{l}}^l + w_{\boldsymbol{u}}^j w_{\boldsymbol{k}}^k \frac{\partial w_{\boldsymbol{l}}^l}{\partial \varphi^p} \right), \tag{G 13}$$

where the partial derivative $\frac{\partial w_{\boldsymbol{u}}^j}{\partial \varphi^p}$ is defined as follows:

$$\frac{\partial w_{\boldsymbol{u}}^j}{\partial \varphi^p} = \begin{cases} 1 & \text{if } |\boldsymbol{u}|_1 = 1 \quad \text{and} \quad p = j, \\ 0 & \text{otherwise.} \end{cases} \tag{G 14}$$

The same applies to all the other partial derivatives in equation (G 13). As before, the product $\boldsymbol{v}^T \frac{\partial \boldsymbol{f}_{\boldsymbol{m}}}{\partial \boldsymbol{\varphi}}$ is computed and stored instead of the full derivative matrix.

The partial derivative of vectors $\boldsymbol{V}_{\boldsymbol{m}}$ and $\dot{\boldsymbol{V}}_{\boldsymbol{m}}$ are

$$\boldsymbol{v}^T \frac{\partial \boldsymbol{V}_{\boldsymbol{m}}}{\partial \boldsymbol{\varphi}} = \sum_{j=1}^{2} \sum_{\substack{\boldsymbol{u},\boldsymbol{k} \in \mathbb{N}^2 \\ 1<u,k<m \\ \boldsymbol{u}+\boldsymbol{k}-\boldsymbol{e}_j=\boldsymbol{m}}} u_j (\boldsymbol{v}^T \boldsymbol{w}_{\boldsymbol{u}}) \frac{\partial R_{\boldsymbol{k}}^j}{\partial \boldsymbol{\varphi}} \tag{G 15}$$

and

$$\boldsymbol{v}^T \frac{\partial \dot{\boldsymbol{V}}_{\boldsymbol{m}}}{\partial \boldsymbol{\varphi}} = \sum_{j=1}^{2} \sum_{\substack{\boldsymbol{u},\boldsymbol{k} \in \mathbb{N}^2 \\ 1<u,k<m \\ \boldsymbol{u}+\boldsymbol{k}-\boldsymbol{e}_j=\boldsymbol{m}}} u_j \left(\boldsymbol{v}^T \frac{\partial \dot{\boldsymbol{w}}_{\boldsymbol{u}}}{\partial \boldsymbol{\varphi}} R_{\boldsymbol{k}}^j + (\boldsymbol{v}^T \dot{\boldsymbol{w}}_{\boldsymbol{u}}) \frac{\partial R_{\boldsymbol{k}}^j}{\partial \boldsymbol{\varphi}} \right), \tag{G 16}$$

where the products $\boldsymbol{v}^T \boldsymbol{w}_{\boldsymbol{u}}$ and $\boldsymbol{v}^T \dot{\boldsymbol{w}}_{\boldsymbol{u}}$ are scalar quantities.

The partial derivative of vector $\boldsymbol{C}_{\boldsymbol{m}}$ is

$$\boldsymbol{v}^T \frac{\partial \boldsymbol{C}_{\boldsymbol{m}}}{\partial \boldsymbol{\varphi}} = -\boldsymbol{v}^T \mathbf{M} \frac{\partial \dot{\boldsymbol{V}}_{\boldsymbol{m}}}{\partial \boldsymbol{\varphi}} - \boldsymbol{v}^T \frac{\partial \boldsymbol{f}_{\boldsymbol{m}}}{\partial \boldsymbol{\varphi}} - \boldsymbol{v}^T (\Lambda_{\boldsymbol{m}} \mathbf{M} + \mathbf{C}) \frac{\partial \boldsymbol{V}_{\boldsymbol{q}}}{\partial \boldsymbol{\varphi}}. \tag{G 17}$$

The partial derivative of the reduced dynamics coefficient is

$$\frac{\partial R_{\boldsymbol{m}}^j}{\partial \boldsymbol{\varphi}} = \frac{\boldsymbol{C}_{\boldsymbol{m}}^T + \boldsymbol{\varphi}^T \frac{\partial \boldsymbol{C}_{\boldsymbol{m}}}{\partial \boldsymbol{\varphi}}}{\Lambda_{\boldsymbol{q}} + \lambda_j + \alpha_R + \beta_R \omega^2}, \tag{G 18}$$

where $\boldsymbol{\varphi}^T \frac{\partial \boldsymbol{C}_{\boldsymbol{m}}}{\partial \boldsymbol{\varphi}}$ is computed using equation (G 17) by setting $\boldsymbol{v} = \boldsymbol{\varphi}$.

The partial derivative of vector $\boldsymbol{D}_m^j$ is

$$\boldsymbol{v}^T \frac{\partial \boldsymbol{D}_m^j}{\partial \boldsymbol{\varphi}} = -\boldsymbol{v}^T[(\Lambda_m + \lambda_j)\mathbf{M} + \mathbf{C}]. \tag{G 19}$$

The partial derivative of the right-hand side of the cohomological equation is

$$\boldsymbol{v}^T \frac{\partial \boldsymbol{h}_m}{\partial \boldsymbol{\varphi}} = -\boldsymbol{v}^T \frac{\partial \boldsymbol{C}_m}{\partial \boldsymbol{\varphi}} - \sum_{j=1}^{2} (\boldsymbol{v}^T \boldsymbol{D}_m^j) \frac{\partial R_m^j}{\partial \boldsymbol{\varphi}} - \sum_{j=1}^{2} \boldsymbol{v}^T \frac{\partial \boldsymbol{D}_m^j}{\partial \boldsymbol{\varphi}} R_m^j, \tag{G 20}$$

where the product $\boldsymbol{v}^T \boldsymbol{D}_m^j$ is a scalar quantity.

The partial derivative of the manifold velocity coefficient is

$$\boldsymbol{v}^T \frac{\partial \dot{\boldsymbol{w}}_m}{\partial \boldsymbol{\varphi}} = (\boldsymbol{v}^T \boldsymbol{\varphi}) \sum_{j=1}^{2} \frac{\partial R_m^j}{\partial \boldsymbol{\varphi}} + \boldsymbol{v}^T \sum_{j=1}^{2} R_m^j + \boldsymbol{v}^T \frac{\partial \boldsymbol{V}_m}{\partial \boldsymbol{\varphi}}, \tag{G 21}$$

where the product $\boldsymbol{v}^T \boldsymbol{\varphi}$ is a scalar quantity.

The partial derivative of the physical amplitude is

$$\frac{\partial x}{\partial \boldsymbol{\varphi}} = \frac{1}{N_\vartheta x} \sum_k x_k^i \boldsymbol{a}^T (\boldsymbol{p}_k^{10} + \boldsymbol{p}_k^{01}), \tag{G 22}$$

where $\boldsymbol{a}$ is a vector such that $a_j = 1$ if $i = j$, 0 otherwise.

The partial derivative of the response frequency is

$$\frac{\partial \Omega}{\partial \boldsymbol{\varphi}} = \frac{1}{2} \mathrm{i} \sum_{m>1} \left(\frac{\partial R_m^2}{\partial \boldsymbol{\varphi}} - \frac{\partial R_m^1}{\partial \boldsymbol{\varphi}} \right) \varrho^{m-1}. \tag{G 23}$$

(d) Partial derivatives with respect to the natural frequency

Here, the partial derivatives are taken with respect to the natural frequency ω, which is a scalar. Therefore, there is no need to multiply the partial derivatives by $\boldsymbol{v}^T$ as done in the previous cases.

The partial derivative of the eigenvalue coefficient is

$$\frac{\partial \Lambda_m}{\partial \omega} = \boldsymbol{m} \cdot \frac{\partial \Lambda}{\partial \omega}, \tag{G 24}$$

where

$$\frac{\partial \Lambda}{\partial \omega} = \begin{bmatrix} \frac{\partial \lambda}{\partial \omega} \\ \frac{\partial \bar{\lambda}}{\partial \omega} \end{bmatrix}, \tag{G 25}$$

$$\frac{\partial \lambda}{\partial \omega} = -\xi - \omega \frac{\partial \xi}{\partial \omega} + \mathrm{i}\sqrt{1-\xi^2} - \mathrm{i}\omega \frac{\xi}{\sqrt{1-\xi^2}} \frac{\partial \xi}{\partial \omega} \tag{G 26}$$

and

$$\frac{\mathrm{d}\xi}{\mathrm{d}\mu} = \frac{\beta_R \omega^2 - \alpha_R}{2\omega^2}. \tag{G 27}$$

The nonlinear force contribution $\boldsymbol{f}_m$ does not depend on the eigenfrequency ω, thus $\frac{\partial \boldsymbol{f}_m}{\partial \omega} = \mathbf{0}$.

The partial derivative of vectors $\boldsymbol{V}_m$ and $\dot{\boldsymbol{V}}_m$ are

$$\frac{\partial \boldsymbol{V}_m}{\partial \omega} = \sum_{j=1}^{2} \sum_{\substack{\boldsymbol{u},\boldsymbol{k} \in \mathbb{N}^2 \\ 1<u,k<m \\ \boldsymbol{u}+\boldsymbol{k}-\boldsymbol{e}_j=\boldsymbol{m}}} u_j \boldsymbol{w}_u \frac{\partial R_k^j}{\partial \omega} \tag{G 28}$$

and

$$\frac{\partial \dot{\boldsymbol{V}}_m}{\partial \omega} = \sum_{j=1}^{2} \sum_{\substack{\boldsymbol{u},\boldsymbol{k}\in\mathbb{N}^2 \\ 1<u,k<m \\ \boldsymbol{u}+\boldsymbol{k}-\boldsymbol{e}_j=\boldsymbol{m}}} u_j \left(\frac{\partial \dot{\boldsymbol{w}}_{\boldsymbol{u}}}{\partial \omega} R_{\boldsymbol{k}}^j + \dot{\boldsymbol{w}}_{\boldsymbol{u}} \frac{\partial R_{\boldsymbol{k}}^j}{\partial \omega} \right). \tag{G 29}$$

The partial derivative of vector $\boldsymbol{C}_m$ is

$$\frac{\partial \boldsymbol{C}_m}{\partial \omega} = -\mathbf{M} \frac{\partial \dot{\boldsymbol{V}}_m}{\partial \omega} - \frac{\partial \boldsymbol{\Lambda}_m}{\partial \omega} \mathbf{M} \boldsymbol{V}_m - (\Lambda_m \mathbf{M} + \mathbf{C}) \frac{\partial \boldsymbol{V}_m}{\partial \omega}. \tag{G 30}$$

The partial derivative of the reduced dynamics coefficient is

$$\frac{\partial R_m^j}{\partial \omega} = \frac{\boldsymbol{\varphi}^T \frac{\partial \boldsymbol{C}_m}{\partial \omega}}{\Lambda_m + \lambda_j + \alpha_R + \beta_R \omega^2} - R_m^j \frac{\frac{\partial \Lambda_m}{\partial \omega} + \frac{\partial \lambda_j}{\partial \omega} + 2\beta_R \omega}{\Lambda_m + \lambda_j + \alpha_R + \beta_R \omega^2}. \tag{G 31}$$

The partial derivative of the right-hand side of the cohomological equation is

$$\frac{\partial \boldsymbol{h}_m}{\partial \omega} = \frac{\partial \boldsymbol{C}_m}{\partial \omega} + \sum_{j=1}^{2} \left(\frac{\partial \boldsymbol{D}_m^j}{\partial \omega} R_m^j + \boldsymbol{D}_m^j \frac{\partial R_m^j}{\partial \omega} \right), \tag{G 32}$$

where

$$\frac{\partial \boldsymbol{D}_m^j}{\partial \omega} = -\left(\frac{\partial \Lambda_m}{\partial \omega} + \frac{\partial \lambda_j}{\partial \omega} \right) \mathbf{M} \boldsymbol{\varphi}. \tag{G 33}$$

The partial derivative of the left-hand side of the cohomological equation is

$$\frac{\partial \mathbf{L}_m}{\partial \omega} = (\mathbf{C} + 2\Lambda_m \mathbf{M}) \frac{\partial \Lambda_m}{\partial \omega}. \tag{G 34}$$

The partial derivative of the manifold velocity coefficient is

$$\frac{\partial \dot{\boldsymbol{w}}_m}{\partial \omega} = \frac{\partial \Lambda_m}{\partial \omega} \boldsymbol{w}_m + \boldsymbol{\varphi} \sum_{j=1}^{2} \frac{\partial R_m^j}{\partial \omega} + \frac{\partial \boldsymbol{V}_m}{\partial \omega}. \tag{G 35}$$

The RMS physical amplitude x does not directly depend on ω, while the partial derivative of the response frequency Ω is

$$\frac{\partial \Omega}{\partial \omega} = \frac{1}{2} \mathrm{i} \left(\frac{\partial \bar{\lambda}}{\partial \omega} - \frac{\partial \lambda}{\partial \omega} \right) + \frac{1}{2} \mathrm{i} \sum_{m>1} \left(\frac{\partial R_m^2}{\partial \omega} - \frac{\partial R_m^1}{\partial \omega} \right) \varrho^{m-1}. \tag{G 36}$$

(e) Partial derivatives with respect to the design variables

Using tensor notation, the partial derivative of the nonlinear force contribution is

$$\frac{\partial f_m^i}{\partial \mu} = \sum_{\substack{\boldsymbol{u},\boldsymbol{k}\in\mathbb{N}^2 \\ \boldsymbol{u}+\boldsymbol{k}=\boldsymbol{m}}} \frac{\partial T_2^{ijk}}{\partial \mu} w_{\boldsymbol{u}}^j w_{\boldsymbol{k}}^k + \sum_{\substack{\boldsymbol{u},\boldsymbol{k},\boldsymbol{l}\in\mathbb{N}^2 \\ \boldsymbol{u}+\boldsymbol{k}+\boldsymbol{l}=\boldsymbol{m}}} \frac{\partial T_3^{ijkl}}{\partial \mu} w_{\boldsymbol{u}}^j w_{\boldsymbol{k}}^k w_{\boldsymbol{l}}^l. \tag{G 37}$$

The partial derivatives of vectors $\boldsymbol{V}_m$ and $\dot{\boldsymbol{V}}_m$ are

$$\frac{\partial \boldsymbol{V}_m}{\partial \mu} = \sum_{j=1}^{2} \sum_{\substack{\boldsymbol{u},\boldsymbol{k}\in\mathbb{N}^2 \\ 1<u,k<m \\ \boldsymbol{u}+\boldsymbol{k}-\boldsymbol{e}_j=\boldsymbol{m}}} \boldsymbol{w}_{\boldsymbol{u}} u_j \frac{\partial R_{\boldsymbol{k}}^j}{\partial \mu} \tag{G 38}$$

and

$$\frac{\partial \dot{\boldsymbol{V}}_m}{\partial \mu} = \sum_{j=1}^{2} \sum_{\substack{\boldsymbol{u},\boldsymbol{k}\in\mathbb{N}^2 \\ 1<u,k<m \\ \boldsymbol{u}+\boldsymbol{k}-\boldsymbol{e}_j=\boldsymbol{m}}} u_j \left[\frac{\partial \dot{\boldsymbol{w}}_{\boldsymbol{u}}}{\partial \mu} R_{\boldsymbol{k}}^j + \dot{\boldsymbol{w}}_{\boldsymbol{u}} \frac{\partial R_{\boldsymbol{k}}^j}{\partial \mu} \right]. \tag{G 39}$$

The partial derivative of vector $\boldsymbol{C}_m$ is

$$\frac{\partial \boldsymbol{C}_m}{\partial \mu} = -\frac{\partial \mathbf{M}}{\partial \mu}\dot{\boldsymbol{V}}_m - \mathbf{M}\frac{\partial \dot{\boldsymbol{V}}_m}{\partial \mu} - (\Lambda_m \mathbf{M} + \mathbf{C})\frac{\partial \boldsymbol{V}_m}{\partial \mu} - \left(\Lambda_m \frac{\partial \mathbf{M}}{\partial \mu} + \frac{\partial \mathbf{C}}{\partial \mu}\right)\boldsymbol{V}_m - \frac{\partial \boldsymbol{f}_m}{\partial \mu}. \tag{G 40}$$

The partial derivative of the reduced dynamics coefficient is

$$\frac{\partial R_m^j}{\partial \mu} = \frac{\boldsymbol{\varphi}^T \frac{\partial \boldsymbol{C}_m}{\partial \mu}}{\Lambda_m + \lambda_j + \alpha_R + \beta_R \omega^2}. \tag{G 41}$$

The partial derivative of the right-hand side of the cohomological equation is

$$\frac{\partial \boldsymbol{h}_m}{\partial \mu} = \frac{\partial \boldsymbol{C}_m}{\partial \mu} + \sum_{j=1}^{2}\left(\frac{\partial \boldsymbol{D}_m^j}{\partial \mu}R_m^j + \boldsymbol{D}_m^j \frac{\partial R_m^j}{\partial \mu}\right), \tag{G 42}$$

where

$$\frac{\partial \boldsymbol{D}_m^j}{\partial \mu} = -\left[(\Lambda_m + \lambda_j)\frac{\partial \mathbf{M}}{\partial \mu} + \frac{\partial \mathbf{C}}{\partial \mu}\right]\boldsymbol{\varphi}. \tag{G 43}$$

The partial derivative of the left-hand side of the cohomological equation is

$$\frac{\partial \mathbf{L}_m}{\partial \mu} = \frac{\partial \mathbf{K}}{\partial \mu} + \Lambda_m \frac{\partial \mathbf{C}}{\partial \mu} + \Lambda_m^2 \frac{\partial \mathbf{M}}{\partial \mu}. \tag{G 44}$$

The partial derivative of the manifold velocity coefficient is

$$\frac{\partial \dot{\boldsymbol{w}}_m}{\partial \mu} = \sum_{j=1}^{2}\frac{\partial R_m^j}{\partial \mu}\boldsymbol{\varphi} + \frac{\partial \boldsymbol{V}_m}{\partial \mu}. \tag{G 45}$$

The RMS physical amplitude x does not directly depend on μ, while the partial derivative of the response frequency Ω is

$$\frac{\partial \Omega}{\partial \mu} = \frac{1}{2}\mathrm{i}\sum_{m>1}\left(\frac{\partial R_m^2}{\partial \mu} - \frac{\partial R_m^1}{\partial \mu}\right)\varrho^{m-1}. \tag{G 46}$$

Appendix H. Topology optimization details

In the standard density-based formulation for topology optimization [25], each element of the finite element grid is assigned a design variable $\mu \in [0, 1]$, representing its material density (0 for void, 1 for solid). To avoid mesh-dependent solutions and prevent grey transition regions, the regularization filter described in [46] is used:

$$\tilde{\mu}_e = \frac{\sum_{j\in\mathcal{N}_e} w_{j,e}\mu_j}{\sum_{j\in\mathcal{N}_e} w_{j,e}} \tag{H 1}$$

and

$$w_{j,e} = R - |\boldsymbol{x}_j - \boldsymbol{x}_e|, \tag{H 2}$$

where $\tilde{\mu}_e$ is the filtered density of the element e, $\mathcal{N}_e$ is a set that contains the indices of the elements that lie within a circle of radius $R_{filt} = 4$ around element e; $w_{j,e}$ is the distance weight, and $\boldsymbol{x}_e$ and $\boldsymbol{x}_j$ are the coordinates of the centroids of elements e and j, respectively.

To promote a 0/1 density distribution, a projection threshold [46] is used:

$$\bar{\mu}_e = \frac{\tanh(\beta\eta) + \tanh(\beta(\tilde{\mu}_e - \eta))}{\tanh(\beta\eta) + \tanh(\beta(1-\eta))}, \tag{H 3}$$

where $\bar{\mu}_e$ is the projected density of element e, and $\beta = 10$ and $\eta = 0.5$ are projection parameters.

The solid isotropic material with penalization scheme [45] is used to obtain the physical densities:

$$\hat{\mu}_e = \hat{\mu}_0 + (1 - \hat{\mu}_0)\bar{\mu}_e^p, \tag{H 4}$$

where $\hat{\mu}_0 = 10^{-6}$ is an arbitrarily small density of the void element, used to prevent singularities in the numerical method, and p is the penalization power that is gradually increased during the optimization, starting from 1.

The physical densities $\hat{\mu}$ are then used to interpolate the material properties, specifically Young's modulus and density:

$$\mathbf{M} = \bigcup_{e=1}^{N_{\text{el}}} \hat{\mu}_e \mathbf{M}_e, \quad \mathbf{K} = \bigcup_{e=1}^{N_{\text{el}}} \hat{\mu}_e \mathbf{K}_e, \; T_2^{ijk} = \bigcup_{e=1}^{N_{\text{el}}} \hat{\mu}_e T_{2e}^{ijk}, \; T_3^{ijkl} = \bigcup_{e=1}^{N_{\text{el}}} \hat{\mu}_e T_{3e}^{ijkl}, \tag{H 5}$$

where N_{el} is the total number of elements and the operator $\bigcup$ represents the finite element assembly across all the elements of the grid. We use the subscript e to denote an entity at the element level.

The filters in equations (H 1), (H 3), and (H 4) do not affect the sensitivity analysis presented in §(a), but they are incorporated in the partial derivatives of the structural matrices and tensors (e.g. [34]).

References

1. Qalandar KR, Strachan BS, Gibson B, Sharma M, Ma A, Shaw SW, Turner KL. 2014 Frequency division using a micromechanical resonance cascade. *Appl. Phys. Lett.* **105**, 244103. (doi:10.1063/1.4904465)
2. Bellet R, Cochelin B, Herzog P, Mattei PO. 2010 Experimental study of targeted energy transfer from an acoustic system to a nonlinear membrane absorber. *J. Sound Vib.* **329**, 2768–2791. (doi:10.1016/j.jsv.2010.01.029)
3. Vakakis AF, Gendelman OV, Bergman LA, Mojahed A, Gzal M. 2022 Nonlinear targeted energy transfer: state of the art and new perspectives. *Nonlinear Dyn.* **108**, 711–741. (doi:10.1007/s11071-022-07216-w)
4. Asadi K, Yeom J, Cho H. 2021 Strong internal resonance in a nonlinear, asymmetric microbeam resonator. *Microsyst. Nanoeng.* **7**, 9. (doi:10.1038/s41378-020-00230-1)
5. Li Z, Xu M, Norte RA, Aragón AM, Steeneken PG, Alijani F. 2024 Strain engineering of nonlinear nanoresonators from hardening to softening. *Commun. Phys.* **7**, 53. (doi:10.1038/s42005-024-01543-7)
6. Zhang W, Baskaran R, Turner KL. 2002 Effect of cubic nonlinearity on auto-parametrically amplified resonant MEMS mass sensor. *Sens. Actuators, A* **102**, 139–150. (doi:10.1016/S0924-4247(02)00299-6)
7. Marconi J, Bonaccorsi G, Giannini D, Falorni L, Braghin F. 2021 Exploiting nonlinearities for frequency-matched mems gyroscopes tuning. In *2021 IEEE Int. Symposium on Inertial Sensors and Systems (INERTIAL)*, pp. 1–4. IEEE. (doi:10.1109/INERTIAL51137.2021.9430478)
8. Tiso P, Mahdiabadi MK, Marconi J. 2021 pp. 97–138. In *Modal methods for reduced order modeling*, pp. 97–138. Berlin, Boston: De Gruyter. (doi:10.1515/9783110498967-004)
9. Touzé C, Vizzaccaro A, Thomas O. 2021 Model order reduction methods for geometrically nonlinear structures: a review of nonlinear techniques. *Nonlinear Dyn.* **105**, 1141–1190. (doi:10.1007/s11071-021-06693-9)
10. Kerschen G, Peeters M, Golinval JC, Vakakis AF. 2009 Nonlinear normal modes, part I: a useful framework for the structural dynamicist. *Mech. Syst. Signal Process.* **23**, 170–194. (doi:10.1016/j.ymssp.2008.04.002)
11. Haller G, Ponsioen S. 2016 Nonlinear normal modes and spectral submanifolds: existence, uniqueness and use in model reduction. *Nonlinear Dyn.* **86**, 1493–1534. (doi:10.1007/s11071-016-2974-z)
12. Breunung T, Haller G. 2018 Explicit backbone curves from spectral submanifolds of forced-damped nonlinear mechanical systems. *Proc. R. Soc. A* **474**, 20180083. (doi:10.1098/rspa.2018.0083)
13. Dankowicz H, Schilder F. 2013 *Recipes for Continuation*. Philadelphia, PA: Society for Industrial and Applied Mathematics.

14. Krack M, Gross J. 2019 *Harmonic balance for nonlinear vibration problems*. Mathematical Engineering. Cham: Springer International Publishing.
15. Kerschen G, Viguié R, Golinval JC, Peeters M, Sérandour G. 2008 Nonlinear normal modes, Part II: Toward a practical computation using numerical continuation techniques. *Mech. Syst. Signal Process.* **23**, 195–216. (doi:10.1016/j.ymssp.2008.04.003)
16. Jain S, Haller G. 2022 How to compute invariant manifolds and their reduced dynamics in high-dimensional finite element models. *Nonlinear Dyn.* **107**, 1417–1450. (doi:10.1007/s11071-021-06957-4)
17. Thurnher T, Haller G, Jain S. 2024 Nonautonomous spectral submanifolds for model reduction of nonlinear mechanical systems under parametric resonance. *Chaos: An Interdiscip. J. Nonlinear Sci.* **34**, 073127 (doi:10.1063/5.0168431)
18. Dou S, Jensen JS. 2016 Optimization of hardening/softening behavior of plane frame structures using nonlinear normal modes. *Comput. Struct.* **164**, 63–74. (doi:10.1016/j.compstruc.2015.11.001)
19. Dou S, Jensen JS. 2015 Optimization of nonlinear structural resonance using the incremental harmonic balance method. *J. Sound Vib.* **334**, 239–254. (doi:10.1016/j.jsv.2014.08.023)
20. Dou S, Strachan BS, Shaw SW, Jensen JS. 2015 Structural optimization for nonlinear dynamic response. *Phil. Trans. R. Soc. A* **373**, 20140408 (doi:10.1098/rsta.2014.0408)
21. Schiwietz D, Hörsting M, Weig EM, Degenfeld-Schonburg P, Wenzel M. 2024 Shape Optimization of Eigenfrequencies in MEMS Gyroscopes. (doi:10.48550/arXiv.2402.05837)
22. Schiwietz D, Hörsting M, Weig EM, Wenzel M, Degenfeld-Schonburg P. 2025 Shape optimization of geometrically nonlinear modal coupling coefficients: an application to MEMS gyroscopes. *Sci. Rep.* **15**, 10957. (doi:10.1038/s41598-025-95412-0)
23. Detroux T, Noël JP, Kerschen G. 2021 Tailoring the resonances of nonlinear mechanical systems. *Nonlinear Dyn.* **103**, 3611–3624. (doi:10.1007/s11071-020-06002-w)
24. Li Z, Alijani F, Sarafraz A, Xu M, Norte RA, Aragón AM, Steeneken PG. 2025 Finite element-based nonlinear dynamic optimization of nanomechanical resonators. *Microsyst. Nanoeng.* **11**, 16. (doi:10.1038/s41378-024-00854-7)
25. Bendsøe MP, Sigmund O. 2004 *Topology optimization: theory, methods, and applications*. Berlin Heidelberg: Springer.
26. Choi W, Park G. 2002 Structural optimization using equivalent static loads at all time intervals. *Comput. Methods Appl. Mech. Eng.* **191**, 2105–2122. (doi:10.1016/S0045-7825(01)00373-5)
27. Kim YI, Park GJ. 2010 Nonlinear dynamic response structural optimization using equivalent static loads. *Comput. Methods Appl. Mech. Eng.* **199**, 660–676. (doi:10.1016/j.cma.2009.10.014)
28. Lee HA, Park GJ. 2015 Nonlinear dynamic response topology optimization using the equivalent static loads method. *Comput. Methods Appl. Mech. Eng.* **283**, 956–970. (doi:10.1016/j.cma.2014.10.015)
29. Lu S, Zhang Z, Guo H, Park GJ, Zuo W. 2021 Nonlinear dynamic topology optimization with explicit and smooth geometric outline via moving morphable components method. *Struct. Multidiscipl. Optim.* **64**, 2465–2487. (doi:10.1007/s00158-021-03000-3)
30. Li Q, Wu Q, Dou S, Wang J, Liu S, Chen W. 2022 Nonlinear eigenvalue topology optimization for structures with frequency-dependent material properties. *Mechan. Syst. Signal Process.* **170**, 108835 (doi:10.1016/j.ymssp.2022.108835)
31. Dalklint A, Wallin M, Tortorelli DA. 2020 Eigenfrequency constrained topology optimization of finite strain hyperelastic structures. *Struct. Multidiscipl. Optim.* **61**, 2577–2594. (doi:10.1007/s00158-020-02557-9)
32. Saccani A, Marconi J, Tiso P. 2022 Sensitivity analysis of nonlinear frequency response of defected structures. *Nonlinear Dyn.* **111**, 4027–4051. (doi:10.1007/s11071-022-08064-4)
33. Pozzi M, Marconi J, Jain S, Braghin F. 2024 Backbone curve tailoring via Lyapunov subcenter manifold optimization. *Nonlinear Dyn.* **112**, 15719–15739. (doi:10.1007/s11071-024-09881-5)
34. Pozzi M, Marconi J, Jain S, Li M, Braghin F. 2025 Topology optimization of nonlinear structural dynamics with invariant manifold-based reduced order models. *Struct. Multidiscipl. Optim.* **68**, 72. (doi:10.1007/s00158-025-04010-1)
35. Li M. 2024 Explicit sensitivity analysis of spectral submanifolds of mechanical systems. *Nonlinear Dyn.* **111**, 4027–4051. (doi:10.1007/s11071-024-09947-4)
36. Marconi J, Tiso P, Braghin F. 2020 A nonlinear reduced order model with parametrized shape defects. *Comput. Methods Appl. Mech. Eng.* **360**, 112785. (doi:10.1016/j.cma.2019.112785)
37. Manzoni A, Quarteroni A, Salsa S. 2021 *Optimal control of partial differential equations*. Cham, Switzerland: Springer Nature.

38. Wirtinger W. 1927 Zur formalen Theorie der Funktionen von mehr komplexen Veränderlichen. *Math. Ann.* **97**, 357–375. (doi:10.1007/BF01447872)
39. Pozzi M, Bonaccorsi G, Braghin F. 2023 A temperature-robust level-set approach for eigenfrequency optimization. *Struct. Multidiscip. Optim.* **66**, 173. (doi:10.1007/s00158-023-03622-9)
40. Jain S, Marconi J, Tiso P. 2022 YetAnotherFEcode. Zenodo. (doi:10.5281/zenodo.7313486)
41. Svanberg K. 1987 The method of moving asymptotes–a new method for structural optimization. *Int. J. Numer. Methods Eng.* **24**, 359–373. (doi:10.1002/nme.1620240207)
42. Morsy AA, Tiso P. 2025 Model reduction for systems with random parameters using spectral submanifolds. *Nonlinear Dyn.* (doi:10.1007/s11071-025-11396-6)
43. Acar C, Shkel A. 2009 *MEMS Vibratory Gyroscopes*. New York, NY: Springer Science+Business Media.
44. Cook RD, Malkus DS, Plesha ME, Witt RJ. 2001 *Concepts and applications of finite element analysis*. John Wiley & Sons.
45. Bendsøe MP, Sigmund O. 1999 Material interpolation schemes in topology optimization. *Arch. Appl. Mech.* **69**, 635–654. (doi:10.1007/S004190050248)
46. Wang F, Lazarov BS, Sigmund O. 2011 On projection methods, convergence and robust formulations in topology optimization. *Struct. Multidiscip. Optim.* **43**, 767–784. (doi:10.1007/s00158-010-0602-y)